nature cancer

ARTICLES

https://doi.org/10.1038/s43018-021-00223-7

Check for updates

Downregulation of the FTO m^{6}A RNA demethylase promotes EMT-mediated progression of epithelial tumors and sensitivity to Wnt inhibitors

Jana Jeschke[1,24], Evelyne Collignon[1,24], Clémence Al Wardi[1,24], Mohammad Krayem[2,24], Martin Bizet[1], Yan Jia[1,3], Soizic Garaud[4], Zéna Wimana[2,5], Emilie Calonne[1], Bouchra Hassabi[1], Renato Morandini[2], Rachel Deplus[1], Pascale Putmans[1], Gaurav Dube[1], Nitesh Kumar Singh[1], Alexander Koch[6], Kateryna Shostak[7], Lara Rizzotto[8], Robert L. Ross[9], Christine Desmedt[10], Yacine Bareche[10], Françoise Rothé[10], Jacqueline Lehmann-Che[11,12], Martine Duterque-Coquillaud[13], Xavier Leroy[13,14], Gerben Menschaert[15], Luis Teixeira[11,12], Mingzhou Guo[16], Patrick A. Limbach[9], Pierre Close[17,18], Alain Chariot[7,18], Eleonora Leucci[8,19], Ghanem Ghanem[2], Bi-Feng Yuan[20], Karen Willard-Gallo[4], Christos Sotiriou[10], Jean-Christophe Marine[21,22] and François Fuks[1,23] ✉

Post-transcriptional modifications of RNA constitute an emerging regulatory layer of gene expression. The demethylase fat mass- and obesity-associated protein (FTO), an eraser of *N*^{6}-methyladenosine (m^{6}A), has been shown to play a role in cancer, but its contribution to tumor progression and the underlying mechanisms remain unclear. Here, we report widespread FTO downregulation in epithelial cancers associated with increased invasion, metastasis and worse clinical outcome. Both in vitro and in vivo, FTO silencing promotes cancer growth, cell motility and invasion. In human-derived tumor xenografts (PDXs), FTO pharmacological inhibition favors tumorigenesis. Mechanistically, we demonstrate that FTO depletion elicits an epithelial-to-mesenchymal transition (EMT) program through increased m^{6}A and altered 3′-end processing of key mRNAs along the Wnt signaling cascade. Accordingly, FTO knockdown acts via EMT to sensitize mouse xenografts to Wnt inhibition. We thus identify FTO as a key regulator, across epithelial cancers, of Wnt-triggered EMT and tumor progression and reveal a therapeutically exploitable vulnerability of FTO-low tumors.

Growing evidence suggests that chemical modifications on RNA, similar to those on DNA or histones, control gene expression[1]. More than 100 types of RNA modifications have been reported[2], among which m^{6}A is the most abundant internal modification[3]. Transcriptome-wide mappings of m^{6}A identified methylated sites in more than 7,000 mRNA transcripts, many conserved between humans and mice[3,4]. Marking with m^{6}A occurs on adenosines embedded in the consensus sequence G(G > A) m^{6}ACU, especially in 3′-untranslated regions (UTRs) near stop codons of transcripts[5]. Installed by the METTL3/METTL14/WTAP methyltransferase complex and erased by the demethylases FTO and ALKBH5 (refs. [6,7]), m^{6}A influences fundamental aspects of mRNA metabolism, such as mRNA stability, splicing, transport and translation, thereby impacting gene expression[3–5,8–12].

FTO was found to catalyze m^{6}A demethylation in an Fe(II)- and α-ketoglutarate-dependent enzymatic reaction[6,13,14]. In addition to an involvement in essential biological processes[5,8], FTO has been linked to cancer, acting as an oncoprotein in leukemia[15,16]. Despite conflicting results by Vu et al., who observed no substantial effect of FTO depletion on acute myeloid leukemia (AML) cell viability[17], the development of FTO inhibitors has since shown encouraging results in preclinical settings[16,18,19]. Similar oncogene functions were

[1]Laboratory of Cancer Epigenetics, Faculty of Medicine, ULB-Cancer Research Center (U-CRC), Université Libre de Bruxelles (ULB), Brussels, Belgium. [2]Laboratory of Oncology and Experimental Surgery, Institut Jules Bordet, ULB, Brussels, Belgium. [3]Department of Breast Oncology, Tianjin Medical University Cancer Institute and Hospital, Tianjin, China. [4]Molecular Immunology Laboratory, Institut Jules Bordet, ULB, Brussels, Belgium. [5]Department of Nuclear Medicine, Institut Jules Bordet, ULB, Brussels, Belgium. [6]Department of Pathology, Maastricht UMC, Maastricht, the Netherlands. [7]Laboratory of Medical Chemistry, GIGA Stem Cells, University of Liège, Liège, Belgium. [8]Trace, LKI Leuven Cancer Institute, KU Leuven, Leuven, Belgium. [9]Rieveschl Laboratories for Mass Spectrometry, Department of Chemistry, University of Cincinnati, Cincinnati, OH, USA. [10]Breast Cancer Translational Research Laboratory, Institut Jules Bordet, U-CRC, ULB, Brussels, Belgium. [11]Pathophysiology of Breast Cancer Team, Université de Paris, INSERM U976, HIPI, Paris, France. [12]Breast Disease Unit and Molecular Oncology Unit, AP-HP, Hôpital Saint-Louis, Paris, France. [13]Université Lille, CNRS, Inserm, CHU Lille, Institut Pasteur de Lille, UMR9020-UMR-S 1277, CANTHER, Lille, France. [14]Department of Pathology, CHU Lille, Université Lille, Lille, France. [15]Biobix, Laboratory of Bioinformatics and Computational Genomics, Ghent University, Ghent, Belgium. [16]Department of Gastroenterology & Hepatology, Chinese PLA General Hospital, Beijing, China. [17]Laboratory of Cancer Signaling, GIGA Stem Cells, University of Liège, Liège, Belgium. [18]WELBIO, University of Liège, Liège, Belgium. [19]Laboratory of RNA Cancer Biology, Department of Oncology, LKI, KU Leuven, Leuven, Belgium. [20]College of Chemistry and Molecular Sciences, Wuhan University, Wuhan, China. [21]Laboratory for Molecular Cancer Biology, VIB, KU Leuven, Leuven, Belgium. [22]Laboratory for Molecular Cancer Biology, Department of Oncology, KU Leuven, Leuven, Belgium. [23]WELBIO, Université Libre de Bruxelles (ULB), Brussels, Belgium. [24]These authors contributed equally: Jana Jeschke, Evelyne Collignon, Clémence Al Wardi, Mohammad Krayem. ✉e-mail: ffuks@ulb.ac.be

assigned to FTO in other cancers, such as glioblastoma and melanoma, highlighting the potential of targeting FTO as a therapeutic strategy against cancer[20,21]. However, seemingly conflicting reports, in which a tumor suppressor role was attributed to FTO in other cancers[22–24], called for caution, and the tissue of origin and cancer subtype should be carefully considered when evaluating clinical implications. Strikingly, both gain and loss of expression have been reported in breast cancer, with various impacts on survival[25–27]. The situation is thus far from clear, and in-depth studies are needed to disentangle the apparent emerging conundrum about the role of FTO in cancer biology, especially in light of ongoing efforts to develop FTO inhibitors as anticancer drugs[18,19]. In the present study, we have sought to provide a better understanding of how FTO affects cancer progression, what the underlying mechanisms are and how the knowledge gained might be exploited clinically.

Results

***FTO* downregulation is widespread in cancers and enhances breast tumorigenesis.** To get a broad view of FTO dysregulation in cancers, we first investigated *FTO* expression in tumor samples from The Cancer Genome Atlas (TCGA) database versus their healthy counterparts. We frequently found significant downregulation of *FTO* in epithelial cancers (bladder, breast, cervix, kidney, lung, prostate, thyroid and uterus) and a non-epithelial cancer type (glioblastoma) (Fig. 1a). This finding prompted us to explore the consequences of *FTO* downregulation in breast cancer, one of the most prevalent and clinically challenging cancer types. We first confirmed downregulation of *FTO* (Extended Data Fig. 1a) and revealed, using mass spectrometry, both reduced m^{6}A methylation in *FTO*-high versus *FTO*-low tumor samples (Fig. 1b) and a higher global level of m^{6}A marking in human breast cancers than in healthy tissues (Extended Data Fig. 1b). Notably, *FTO* downregulation occurred in all major molecular subtypes of breast cancer (Fig. 1c).

We next silenced *FTO* in SKBR3 breast cancer cells, a widely used cellular model of HER2-positive breast cancer. In clonogenic assays, *FTO*-depleted (RNAi) cells (Extended Data Fig. 1c) showed more pronounced colony and mammosphere formation than control cells (Fig. 1d and Extended Data Fig. 1d,e), and this difference depended on FTO catalytic activity (Extended Data Fig. 1f). In immunocompromised mice, *FTO* knockdown markedly enhanced engraftment of SKBR3 cells (Fig. 1e) by affecting proliferation (Ki67) and angiogenesis (CD31) but not apoptosis (cleaved caspase 3) (Fig. 1f). To extend our study of the consequences of *FTO* downregulation to another breast cancer subtype, we conducted functional studies in MCF7 cells, a model of luminal breast cancer. As observed with SKBR3 cells, *FTO* depletion in MCF7 cells resulted in increased clonogenicity and enhanced engraftment in immunocompromised mice (Fig. 1g,h and Extended Data Fig. 1g). FTO can thus play a tumor-suppressive role in breast cancer cells, and this depends on its m^{6}A demethylation activity.

***FTO* depletion promotes tumor progression and metastasis in breast cancer.** Cancer stem cells can disseminate and have been linked to both tumor relapse and metastatic dissemination[28]. This, and the increased ability of *FTO*-knockdown cancer cells to form mammospheres (Fig. 1d,g), led us to speculate that *FTO* loss might favor breast tumor progression. In real-time chemotaxis assays, we found *FTO*-depleted SKBR3 cells to display a greater ability to migrate and invade than control cells (Fig. 2a and Extended Data Fig. 2a–c), and this difference was not confounded by differences in proliferation or viability (Extended Data Fig. 2d) but depended on FTO catalytic activity (Extended Data Fig. 2e). We further performed chemotaxis assays with MCF7 breast cancer cells and, as in the case of SKBR3 cells, *FTO* depletion accelerated migraton of these cells (Fig. 2b).

To substantiate these findings in vivo, we assessed tumor engraftment in a PDX model of luminal breast cancer, a process linked to clinical parameters of cancer progression[29]. Strikingly, treatment with the FTO inhibitor meclofenamic acid (MA)[30] substantially enhanced primary breast tumor engraftment in this highly relevant preclinical model expressing the FTO protein (Fig. 2c and Extended Data Fig. 2f). We then used positron emission tomography (PET) with fluorine-18 fluorodeoxyglucose (^{18}F-FDG) to measure metabolic activity in mice xenograft tumors, as increased ^{18}F-FDG uptake has been found to correlate with markers of tumor progression in various cancer types, including breast cancer[31,32]. We observed higher metabolic activity in *FTO*-depleted tumors than in control tumors, indicative of a more progressive phenotype (Fig. 2d). We additionally measured increased ^{18}F-FDG uptake by locoregional subiliac lymph nodes (LNs) in mice bearing *FTO*-depleted tumors compared to mice with control xenografts (Extended Data Fig. 2g). Consistent with our findings from SKBR3 xenografts, ^{18}F-FDG uptake was increased in the lungs and livers of mice injected in the tail vein with *FTO*-depleted SKBR3 cells compared to in mice injected with control SKBR3 cells, indicative of the formation of micrometastases (Fig. 2e). Together, our data indicate that downregulation of *FTO* promotes cancer cell aggressiveness, invasion and metastasis in vivo.

In keeping with the above results, individuals with breast cancer showed an inverse correlation between *FTO* expression and

Fig. 1 | *FTO* loss enhances breast tumorigenesis. a, Downregulation of *FTO* expression in several cancers (red) versus healthy tissues (green) in TCGA. The number of samples (*N*) is indicated below each tissue type. *P* values were calculated by two-tailed *t*-test. Effect size was estimated by Cohen's distance: $d_{bladder}=0.61$, $d_{breast}=1.39$, $d_{cervix}=1.49$, $d_{glioblastoma}=1.57$, $d_{kidney}=2.22$, $d_{lung}=0.98$, $d_{prostate}=0.90$, $d_{thyroid}=1.06$, $d_{uterine}=1.36$; FPKM, fragments per kilobase of transcript per million. **b**, Global m^{6}A levels by mass spectrometry in human breast cancer biopsies with low ($n=25$) or high ($n=15$) *FTO* expression; *P* value calculated by two-tailed *t*-test ($P=0.0029$); BC, breast cancer. **c**, Downregulation of *FTO* expression in breast cancer subtypes compared to healthy breast in TCGA. The number of samples (*n*) is indicated for each group. *P* values were calculated by two-tailed *t*-test (versus healthy breast), as indicated; red, basal-like; pink, HER2-like; dark blue, luminal A; light blue, luminal B; gray, healthy breast. **d**, Effects of *FTO* knockdown by short hairpin RNA (shRNA) on colony-forming capacity (colony-forming units (c.f.u.), left; $P=0.0003$) and mammosphere-forming capacity (right; $P=0.03$) in SKBR3 cells. Data are from $n=3$ technical replicates (mean + s.d.) within a single experiment and are representative of three biologically independent experiments provided as source data. *P* values were calculated by two-tailed *t*-test; Ctrl, control; RNAi, RNA interference. **e**, *FTO* depletion enhances tumor engraftment in nude mice subcutaneously injected with SKBR3 breast cells ($n=6$ tumors per group; mean ± s.e.m., $P=0.0052$, two-way analysis of variance (ANOVA)). **f**, Immunohistochemistry (IHC) analysis of tumors from SKBR3 xenografts from **e** at the experiment end point. Representative images of tissue sections are shown. Percent Ki67-, CASP3- and CD31-positive cells are depicted ($n=3$ fields × 3 tumors per group; mean + s.e.m.). *P* values were calculated by two-tailed *t*-test ($P_{Ki67}<0.0001$; $P_{CASP3}=0.5$; $P_{CD31}=0.0007$); H&E, hematoxylin and eosin. **g**, Effects of *FTO* knockdown on colony-forming capacity (top; $P=0.0004$) and mammosphere-forming capacity (bottom; $P=0.006$) in MCF7 cells. Data are from $n=3$ technical replicates (mean + s.d.) within a single experiment and are representative of two biologically independent experiments provided as source data. *P* values were calculated by two-tailed *t*-test. **h**, Nude mice were injected as indicated in **e** with MCF7 breast cells ($n=6$ tumors per group; mean ± s.e.m., $P<0.0001$, two-way ANOVA). Boxes in the box plots of **a**–**c** define the interquartile range (IQR) split by the median, with whiskers extending to the most extreme values within 1.5 × IQR beyond the box.

tumor grade, LN invasion and distant metastasis-free survival in a meta-analysis of public data ('KM cohort'; see Methods section and Fig. 2f). We validated the inverse correlation between *FTO* expression and survival in the METABRIC breast cancer cohort (Extended Data Fig. 2h) and in several individual datasets of the aggregate KM cohort (Extended Data Fig. 2i).

The role of FTO as a tumor suppressor extends to other epithelial cancers. To test whether our findings in breast cancer could be extended to other tumors, we focused on another prevalent cancer type, prostate cancer, in which we found *FTO* expression to be downregulated (Fig. 1a). In human prostate cancer biopsies, we observed an inverse correlation between *FTO* loss and high global

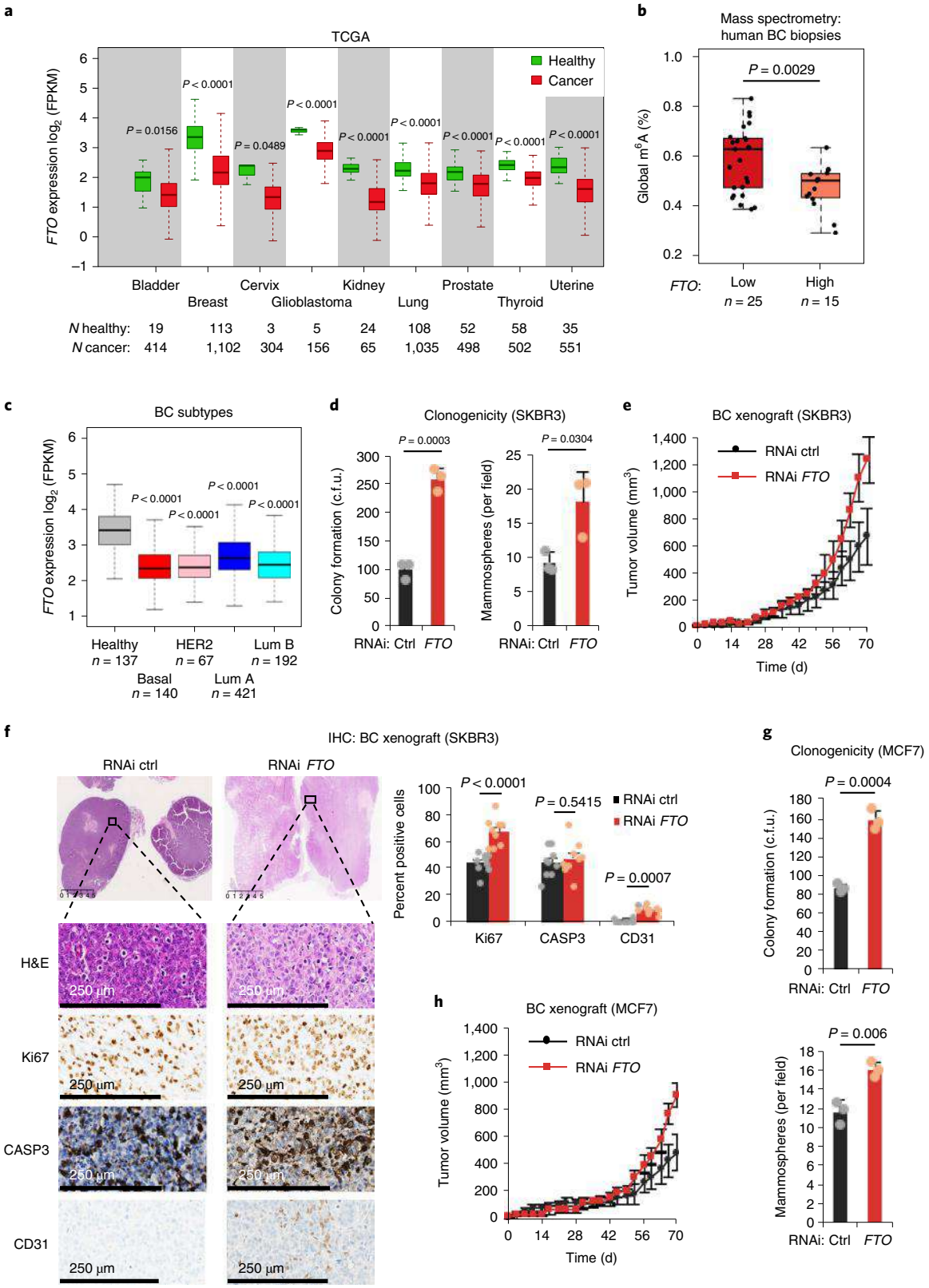

m^{6}A (Fig. 3a). Silencing *FTO* in the PC3 prostate cancer cell line (Extended Data Fig. 3a) enhanced tumorigenicity in vitro (Fig. 3b) and accelerated xenograft tumor growth in immunocompromised mice (Extended Data Fig. 3b). As expected, PC3 cell motility was also increased following *FTO* knockdown (Fig. 3c and Extended Data Fig. 3c). These observations were further extended to cervical and lung cancer, as *FTO*-depleted Ca Ski and H1650 cells displayed similar phenotypes (Fig. 3d,e and Extended Data Fig. 3d–f). Consistent with these phenotypes, we observed an inverse correlation between *FTO* expression and disease progression or clinical outcome in public datasets of prostate cancer (Fig. 3f) and in lung and uterus cancers (Extended Data Fig. 3g,h). To further substantiate these data, we performed tail vein injections with PC3 cells in immunocompromised mice to generate a metastatic prostate cancer model. ^{18}F-FDG uptake was increased in the lungs and livers of mice injected with *FTO*-depleted PC3 cells compared to control PC3 cells (Fig. 3g). Together, these results echo those obtained in breast cancer. We therefore conclude that low *FTO* expression correlates with an invasive and metastatic phenotype in various epithelial cancers.

***FTO* loss elicits an EMT program.** To expose the mechanism(s) through which *FTO* loss favors an invasive and metastatic phenotype, we applied gene set enrichment analysis (GSEA) to data obtained by RNA sequencing (RNA-seq) and identified 'Epithelial Mesenchymal Transition' as one of the top overrepresented gene sets in *FTO*-depleted cells (Fig. 4a and Supplementary Table 1). Accordingly, we found increased expression of mesenchymal genes and decreased expression of epithelial genes in RNAi *FTO* compared to RNAi control SKBR3 cells (Fig. 4b). These results strongly suggest that FTO acts as a modulator of EMT. Following *FTO* depletion, we observed morphological changes associated with EMT (Extended Data Fig. 4a) as well as increased levels of transcripts encoding the mesenchymal markers SNAI2 (SLUG), VIM, FN1, NT5E, SNAI1 (SNAIL), MMP2 and ZEB1 and decreased levels of transcripts encoding the epithelial markers FSTL3, KRT18 and TJP1 (ZO-1) by quantitative PCR with reverse transcription (RT–qPCR) (Fig. 4c). Consistently, we found, by western blotting, increased expression of FN1, VIM and MMP2 in *FTO*-depleted SKBR3 cells (Extended Data Fig. 4b). In *FTO*-depleted tumors from xenografts, western blotting likewise revealed upregulated levels of FN1, VIM and SNAIL proteins (Fig. 4d). We confirmed this finding for FN1 and VIM by IHC (Extended Data Fig. 4c). *FTO* downregulation thus promotes EMT in both cultured cancer cells and in in vivo xenograft tumors. Strikingly, *FTO* depletion resulted in an EMT phenotype comparable to that induced by TGF-β (Extended Data Fig. 4d,e). We further observed EMT activation following *FTO* depletion in MCF7 breast cancer cells and also in prostate and lung cancer cell lines (PC3 and H1650, respectively) (Fig. 4e and Extended Data Fig. 4f,g). Likewise, by IHC, we detected increased expression of VIM in *FTO*-low PC3 xenografts (Extended Data Fig. 4h). In line with the above results, in human tumor biopsies from TCGA, *FTO* was found to be significantly downregulated in EMT-high breast, prostate and other epithelial cancers (Fig. 4f–h). All these data point to FTO as a previously unrecognized negative regulator of EMT, and this may explain the unfavorable consequences of *FTO* downregulation in many cancers.

***FTO* controls Wnt signaling in cancer.** To identify critical downstream signaling pathways through which FTO controls EMT, we generated transcriptome-wide m^{6}A profiles of *FTO*-knockdown and control SKBR3 cells. We identified 1,757 peaks distributed among 1,338 transcripts, with changed m^{6}A levels in *FTO*-depleted versus control cells (Extended Data Fig. 5a and Supplementary Table 2). Gene ontology (GO) analysis with identified FTO targets, that is, transcripts having gained m^{6}A following *FTO* depletion, revealed that among the top ten pathways, several have a well-established role in breast cancer, such as Wnt/β-catenin, p53 and TGF-β[33,34] (Fig. 5a and Supplementary Table 2). These data suggest that FTO controls critical breast cancer pathways through m^{6}A demethylation of RNA.

To investigate the molecular mechanisms underlying the observed effects of *FTO* downregulation (Figs. 1–4), we focused on the Wnt/β-catenin pathway, the most overrepresented among the FTO targets, for in-depth analysis. At every level of the canonical β-catenin-dependent Wnt signaling cascade, we detected key transcripts targeted by FTO (Fig. 5b,c and Extended Data Fig. 5b). In contrast to a previous report, *CTNNB1* (β-catenin) mRNA was not detected as a direct FTO target[35] (Extended Data Fig. 5c and Supplementary Table 2). An FTO target we also identified was *WNT5A*, a transcript commonly associated with non-canonical Wnt signaling[36] but also with β-catenin-dependent signaling activity in various contexts[37,38] (Extended Data Fig. 5d). To see if FTO modulates canonical Wnt signaling, we performed western blot analyses and observed increased stabilization of β-catenin in *FTO*-knockdown SKBR3 cells (Fig. 5d and Extended Data Fig. 5e). Western blotting with total β-catenin antibody applied to nuclear and cytoplasmic fractions of SKBR3 cells revealed an increase of the 'free' signaling pool of β-catenin, as stabilization of β-catenin was observed in nuclear extracts of *FTO*-depleted versus control cells (Extended Data Fig. 5f). Consistently, we observed by immunofluorescence enhanced levels of nuclear β-catenin in *FTO*-depleted SKBR3 cells (Extended Data Fig. 5g). In line with these results, *FTO* depletion caused increased canonical Wnt signaling-dependent transcriptional activity, as evidenced by RT–qPCR quantitation of Wnt/β-catenin target gene transcripts (Extended Data Fig. 5h) and by increased TOPFlash β-catenin/TCF–LEF reporter activity[39] (Fig. 5e). Among our Wnt-related FTO targets, Wnt stimulators (for example, *FZD1*, *WNT5A* and *MARK2*) correlated positively and Wnt inhibitors (for example, *AXIN1* and *CSNK1D*) correlated

Fig. 2 | *FTO* loss promotes breast cancer cell motility and metastases. a,**b**, Real-time chemotactic migration of *FTO*-depleted (red) and control (green) SKBR3 (**a**) or MCF7 (**b**) cells. Data are from $n=3$ technical replicates (mean + s.d.) within a single experiment and are representative of three biologically independent experiments. Independent repeats have been deposited on the Figshare repository (Figshare, https://doi.org/10.6084/m9.figshare.14602932). **c**, Breast tumor PDXs in nude mice (pre)treated with either control vehicle (black) or the FTO inhibitor MA (red; $n=3$ tumors per group, mean ± s.e.m., $P=0.01$ tested by mixed effects model via restricted maximum likelihood). **d**, Tumor metabolism imaging with ^{18}F-FDG PET of xenograft mouse models bearing RNAi control (black; $n=4$) or RNAi *FTO* (red; $n=5$) SKBR3 tumors. Representative ^{18}F-FDG PET–computed tomography (CT) images (9 weeks after inoculation) are shown (pathological uptake in tumors is circled; physiological uptake in brain (B), kidneys (K), bladder (Bl), brown fat (F) and muscle (M)). Quantification of tumor metabolism is presented as the ^{18}F-FDG uptake in maximum standardized uptake values (SUV_{max}). The *P* value was calculated by two-tailed *t*-test ($P=0.03$). **e**, *FTO* depletion increases metastatic burden following tail vein injection of SKBR3 cells. Metabolic activity in the lung and liver of mice bearing either an RNAi control ($n_{lung}=13$, $n_{liver}=14$) or a RNAi *FTO* tumor ($n_{lung}=14$, $n_{liver}=14$) was quantified on the basis of ^{18}F-FDG uptake into SUV_{max} (uptake in liver (Li), lung (Lu), physiological uptake in heart (H), gallbladder (G)). *P* values were calculated by two-tailed *t*-test ($P_{lung}=0.043$; $P_{liver}=0.009$). **f**, Box plot displaying median *FTO* expression according to the tumor grade (left; Kruskal–Wallis test, $P=1.33\times10^{-8}$) or to LN invasion (middle; Wilcoxon test, $P=6.82\times10^{-6}$). Kaplan–Meier analysis was based on *FTO* expression and distant metastasis-free survival in individuals with breast cancer (right; $n_{high\ FTO}=594$, $n_{low\ FTO}=577$; logrank test, $P=0.0009$). Boxes in the box plots in **d**–**f** define the IQR split by the median, with whiskers extending to the most extreme values within 1.5 × IQR beyond the box.

inversely with mesenchymal EMT markers (Fig. 5f). This indicates that EMT may be triggered through FTO-mediated upregulation of canonical Wnt signaling. In support of our results in SKBR3 cells, we observed, by western blotting and IHC, stabilization of β-catenin in mouse xenografts grown from SKBR3 *FTO*-knockdown cells (Fig. 5g and Extended Data Fig. 5i).

We next profiled the m^{6}A mRNA landscape in three human breast tumor biopsies. GO analysis applied to the corresponding m^{6}A peaks (Extended Data Fig. 5j and Supplementary Table 3) revealed Wnt/β-catenin signaling as the top overrepresented pathway (Fig. 5h and Extended Data Fig. 5k). In publicly available data on breast cancer biopsies, *FTO* expression was found to correlate

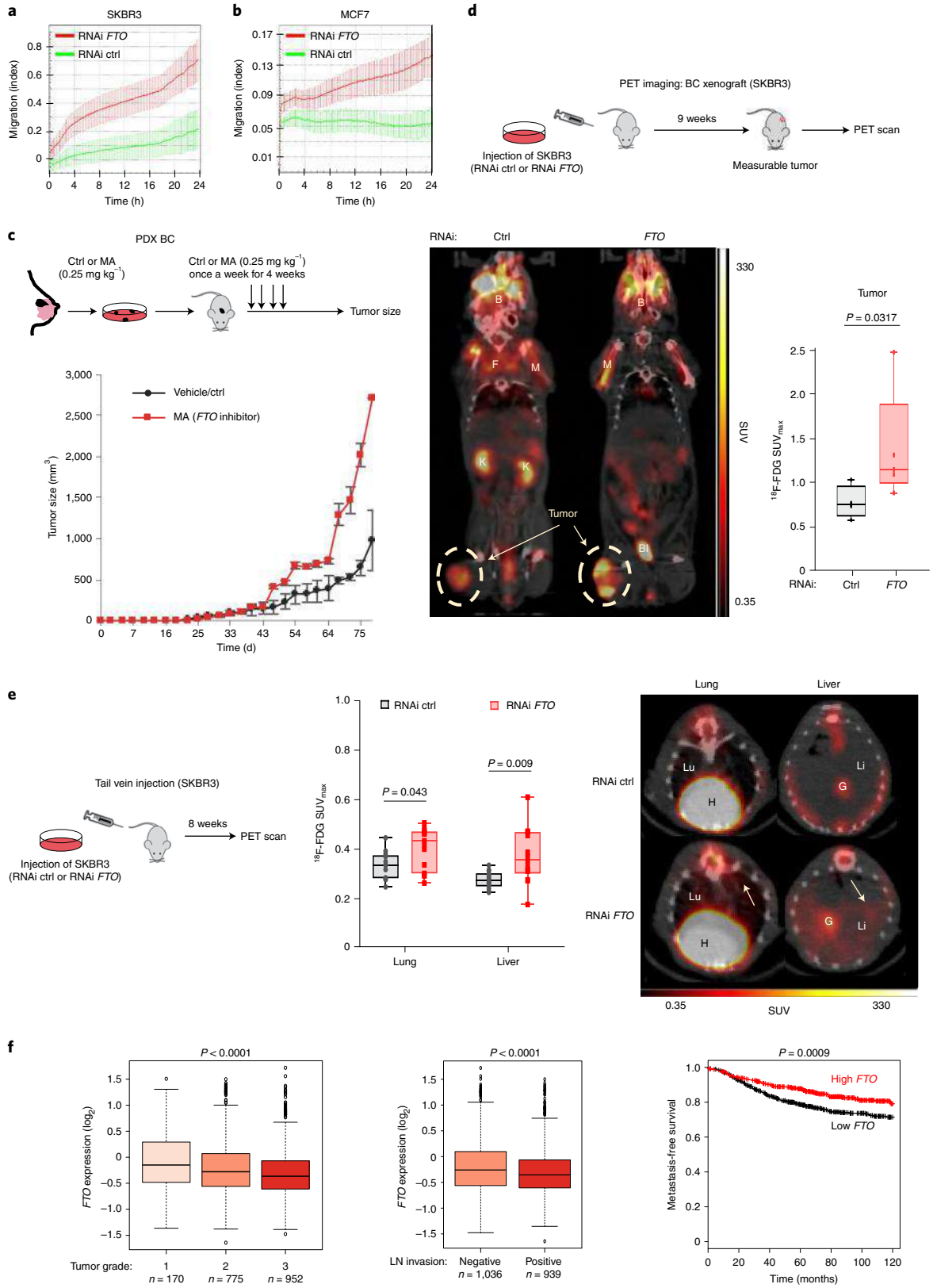

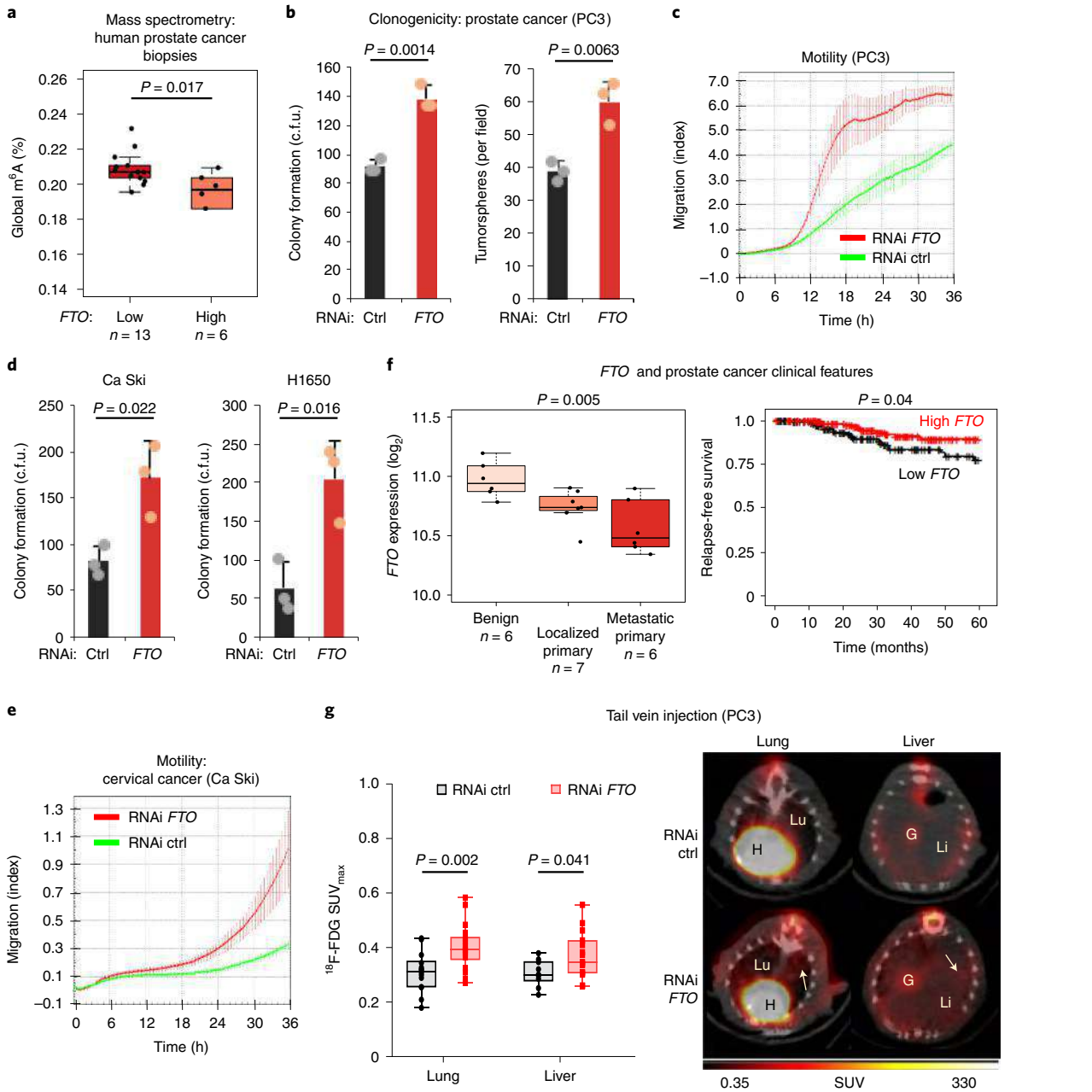

Fig. 3 | *FTO* loss promotes tumor progression in several cancers. a, Global m^{6}A levels by mass spectrometry in human prostate cancer biopsies with low ($n=13$) or high ($n=6$) *FTO* expression; *P* value calculated by two-tailed *t*-test ($P=0.017$). **b**, Effects of *FTO* knockdown on colony-forming capacity (left; $P=0.001$) and tumorsphere-forming capacity (right; $P=0.006$) in PC3 prostate cancer cells; *P* value calculated by two-tailed *t*-test. **c**, Real-time chemotactic migration of *FTO*-depleted (red) and control (green) PC3 cells. **d**, Effects of *FTO* knockdown on colony-forming capacity in Ca Ski cervical cancer cells (left; $P=0.022$) and H1650 lung cancer cells (right; $P=0.016$); *P* values calculated by two-tailed *t*-test. **e**, Real-time chemotactic migration of *FTO*-depleted (red) and control (green) Ca Ski cells. **f**, Box plot displaying *FTO* expression in human biopsies of benign ($n=6$), localized ($n=7$) and metastatic primary ($n=6$) prostate tumors (left; one-way ANOVA, $P=0.005$). Kaplan–Meier analysis showing relapse-free survival for individuals with prostate cancer from TCGA according to the level of tumoral *FTO* expression (right; $n_{high\ FTO}=174$, $n_{low\ FTO}=174$; logrank test, $P=0.04$). **g**, *FTO* depletion increases metastatic burden in tail vein injection of PC3 cells. Metabolic activity in the lung and liver of mice bearing either an RNAi control ($n_{lung}=14$, $n_{liver}=10$) or an RNAi *FTO* tumor ($n_{lung}=18$, $n_{liver}=15$) quantified on the basis of ^{18}F-FDG uptake into SUV_{max} (uptake in liver (Li), lung (Lu), physiological uptake in heart (H), gallbladder (G)); *P* values calculated by two-tailed *t*-test ($P_{lung}=0.002$; $P_{liver}=0.04$). Boxes in the box plots in **a**,**f**, and **g** define the IQR split by the median, with whiskers extending to the most extreme values within 1.5 × IQR beyond the box. Clonogenicity and motility data in **b**–**e** are from $n=3$ technical replicates (mean + s.d.) within a single experiment and are representative of three biologically independent experiments provided as source data for clonogenicity experiments. For motility assays in **c** and **e**, independent repeats have been deposited on the Figshare repository (Figshare, https://doi.org/10.6084/m9.figshare.14602944).

inversely with the level of β-catenin assessed by IHC[40] (Fig. 5i). *FTO* level and canonical Wnt signaling are thus anticorrelated in human breast cancer. When m^{6}A sequencing (m^{6}A-seq) profiling was applied to *FTO*-knockdown PC3 prostate cancer cells, we again found mRNAs encoding key players of Wnt/β-catenin signaling among the FTO targets (Extended Data Fig. 6a,b and Supplementary Table 4).

In line with these data, we observed increased canonical Wnt signaling in *FTO*-depleted PC3 and MCF7 cells by RT–qPCR and in *FTO*-low PC3 xenografts by IHC (Fig. 5j,k and Extended Data Fig. 6c).

Wnt signaling is regulated by FTO-dependent m^{6}A demethylation. To understand how FTO-dependent m^{6}A demethylation affects mRNA function to control Wnt signaling, we focused particularly on *CSNK1D* and *WNT5A*. In contrast to CSNK1D, whose levels decreased upon FTO depletion (Fig. 6a and Extended Data Fig. 6d,e), WNT5A appeared upregulated in *FTO* RNAi cells (Fig. 6a). Given the role of FTO in 3′-end processing[41], we investigated alternative polyadenylation by systematically comparing 3′-UTR lengths in *FTO*-depleted and control SKBR3 cells. Strikingly, several Wnt pathway-related FTO targets appeared in the list of transcripts showing a change in 3′-UTR length following *FTO* depletion, including *SOX11*, *CSNK1D* and *WNT5A* mRNAs (Fig. 6b,c and Supplementary Table 1). Transcript stability can be regulated through binding of microRNAs and RNA-binding proteins to the 3′-UTR[42]. We accordingly observed changes in gene expression for 9 of 21 Wnt-related FTO targets, which were partly explainable by changes in mRNA stability (Fig. 6d,e). Thus, changes in 3′-UTR length affecting *CSNK1D* and *WNT5A* transcripts in *FTO*-knockdown cells may explain the altered levels of the corresponding transcripts and proteins in these cells. FTO may thus control Wnt signaling through 3′-end processing of several of its key components.

***FTO* depletion confers sensitivity to pharmacological Wnt inhibition.** The above data led us to hypothesize that *FTO*-low tumors might be particularly sensitive to Wnt pathway antagonists. To test this, we first compared the responses of cultured RNAi *FTO* and control SKBR3 cells to treatment with a small-molecule inhibitor of nuclear β-catenin called 'inhibitor of β-catenin responsive transcription-3' (iCRT3)[43]. Because iCRT3 inhibits canonical Wnt signaling at the most downstream level by interfering with the T-cell factor (TCF)/β-catenin complex, it enabled us to evaluate the overall effect of FTO on Wnt signaling, resulting from its combined effects on all targets along the canonical Wnt cascade (Fig. 5b). Following iCRT3 treatment, we observed reduced expression of the Wnt/β-catenin target genes *AXIN2* and *TCF1* and reduced Wnt signaling activity in both RNAi control and RNAi *FTO* cells, confirming the efficacy of Wnt inhibition (Extended Data Fig. 7a,b).

To test whether Wnt inhibition could reverse the phenotype of *FTO* depletion, we measured mammosphere formation and chemotactic invasion in iCRT3-treated SKBR3 cells. In *FTO*-depleted cells, but not control cells, iCRT3 substantially reduced mammosphere formation and migration (Fig. 7a,b). We further show in MTT assays that cell proliferation and/or viability were affected by Wnt inhibition (Fig. 7c), but, importantly, even after correction for observed differences in proliferation/cell viability, RNAi *FTO* cells treated with iCRT3 exhibited reduced migration (Extended Data Fig. 7c). Together, these results suggest that Wnt activation plays an important role in the phenotype of *FTO* depletion, and that *FTO* depletion sensitizes SKBR3 cells to Wnt inhibition. Moreover, Wnt inhibition drastically reduced levels of the mesenchymal marker proteins FN1, VIM and SNAIL in *FTO*-depleted cells specifically, suggesting that EMT is triggered through FTO-mediated upregulation of canonical Wnt signaling (Extended Data Fig. 7d). Similar results were obtained following iCRT3 treatment of *FTO*-depleted PC3 prostate cancer cells (Fig. 7d). *FTO* depletion thus enhances the sensitivity of cancer cells to the Wnt inhibitor iCRT3.

***FTO*-low tumors are sensitive to Wnt inhibitor therapy.** To confirm the above data in vivo, we injected athymic mice subcutaneously with either *FTO*-depleted or control SKBR3 cells and, when the tumors reached a measurable size, the mice received intraperitoneal (i.p.) injections of either iCRT3 or DMSO (Fig. 8a). During follow-up, iCRT3-treated control tumors showed only slightly reduced growth compared to their mock-treated counterparts (Fig. 8b, left). *FTO*-depleted tumors, in remarkable contrast, showed drastically stalled growth in response to treatment (Fig. 8b, right). *FTO* depletion thus strongly potentiated the growth-inhibiting effect of iCRT3 on xenograft tumors. When ^{18}F-FDG PET was used to assess metabolic activity in these tumors, we observed no difference between iCRT3-treated and mock-treated control tumors (Fig. 8c, top left), but a significant difference was observed between iCRT3-treated and mock-treated *FTO*-depleted tumors (Fig. 8c, bottom left). Most strikingly, when we measured ^{18}F-FDG uptake by locoregional subiliac LNs (Fig. 8c, right) in the different groups of mice, in mice bearing *FTO*-depleted tumors, we observed a significant decrease (to below the detection limit) in response to iCRT3 treatment (Fig. 8c, bottom right) as opposed to no effect in control tumor-bearing mice (Fig. 8c, top right). In keeping with the above-established link between FTO and EMT, iCRT3 treatment reduced the level of EMT marker FN1 in *FTO*-depleted, but not control, tumors (Extended Data Fig. 7e). To generalize these findings, we treated mice bearing tumors grown from RNAi control or RNAi *FTO* PC3 cells with iCRT3. We again observed enhanced sensitivity of *FTO*-depleted tumors, but not control tumors, to Wnt inhibition (Fig. 8d). Together, these data demonstrate that *FTO* downregulation makes epithelial cancer cells more vulnerable to Wnt inhibition. This vulnerability is lost with Wnt antagonists targeting the Wnt pathway above the level of FTO, as evidenced by the treatment of SKBR3 xenografts with LGK974 (Extended Data Fig. 7f). Thus, *FTO* downregulation sensitizes specifically to the iCRT3 mode of action. This is further supported by our observation that treatment of SKBR3 xenografts with the HER2 inhibitor trastuzumab is equally effective in RNAi control and RNAi *FTO* tumors (Extended Data Fig. 7g).

Discussion

The present study identifies the m^{6}A demethylase FTO as a previously unrecognized regulator of EMT and cancer progression. Furthermore, we provide proof-of-concept evidence that *FTO*-low

Fig. 4 | *FTO* loss elicits an EMT program. a, GSEA from RNA-seq data ($n=5$ per group) in *FTO*-depleted versus control SKBR3 cells; FDR, false discovery rate; NES, normalized enrichment score. **b**, Heat map showing expression changes (Δz score (RNAi *FTO* – RNAi control)) for genes of the EMT hallmark signature from **a** ($P<0.05$ by two-tailed paired *t*-test) in $n=5$ paired replicates of SKBR3 cells. **c**, Relative gene expression of epithelial (top) and mesenchymal (bottom) EMT marker genes measured by RT–qPCR in SKBR3 cells following *FTO* RNAi; data are shown as mean + s.d. normalized to *ACTB* and *SDHA*; $n=7$ independent replicates (except for $n_{SNAI2}=6$ and $n_{ZEB1}=5$); *P* values calculated by two-tailed *t*-test as indicated. **d**, Western blot of EMT markers in RNAi *FTO* versus RNAi control tumors issued from SKBR3 xenografts in mice ($n=4$ per group), with β-actin as a loading control. **e**, Relative gene expression of epithelial (left) and mesenchymal (right) EMT marker genes, as measured by RT–qPCR in PC3 cells following *FTO* RNAi; data are shown as mean + s.d. normalized to *ACTB* and *SDHA*; $n=5$ independent replicates (except for $n_{TWIST1}=4$); *P* values calculated by two-tailed *t*-test. **f**–**h**, Box plots displaying *FTO* expression in human tumors (TCGA) with low or high EMT signature scores in breast cancer (**f**; $P<0.0001$), prostate cancer (**g**; $P<0.0001$) and, from left to right, cervical squamous cell carcinoma ($n=61$ per group), glioblastoma ($n=31$ per group), lung adenocarcinoma and squamous cell carcinoma ($n=205$ per group), thyroid carcinoma ($n=101$ per group) and uterine corpus endometrial carcinoma ($n=110$ per group) (**h**). Boxes define the IQR split by the median, with whiskers extending to the most extreme values within 1.5 × IQR beyond the box; *P* values calculated by two-tailed *t*-test, as indicated.

tumors are likely to benefit from Wnt inhibitor treatment. Our focus here has been mainly on breast and prostate cancer, but our conclusions extend to other epithelial cancers as well.

Both promoter and suppressor roles have been attributed to FTO in breast cancer. In contrast to studies proposing an oncogenic role for FTO[12,25,27,44], but in line with the observation of Wu et al.[26],

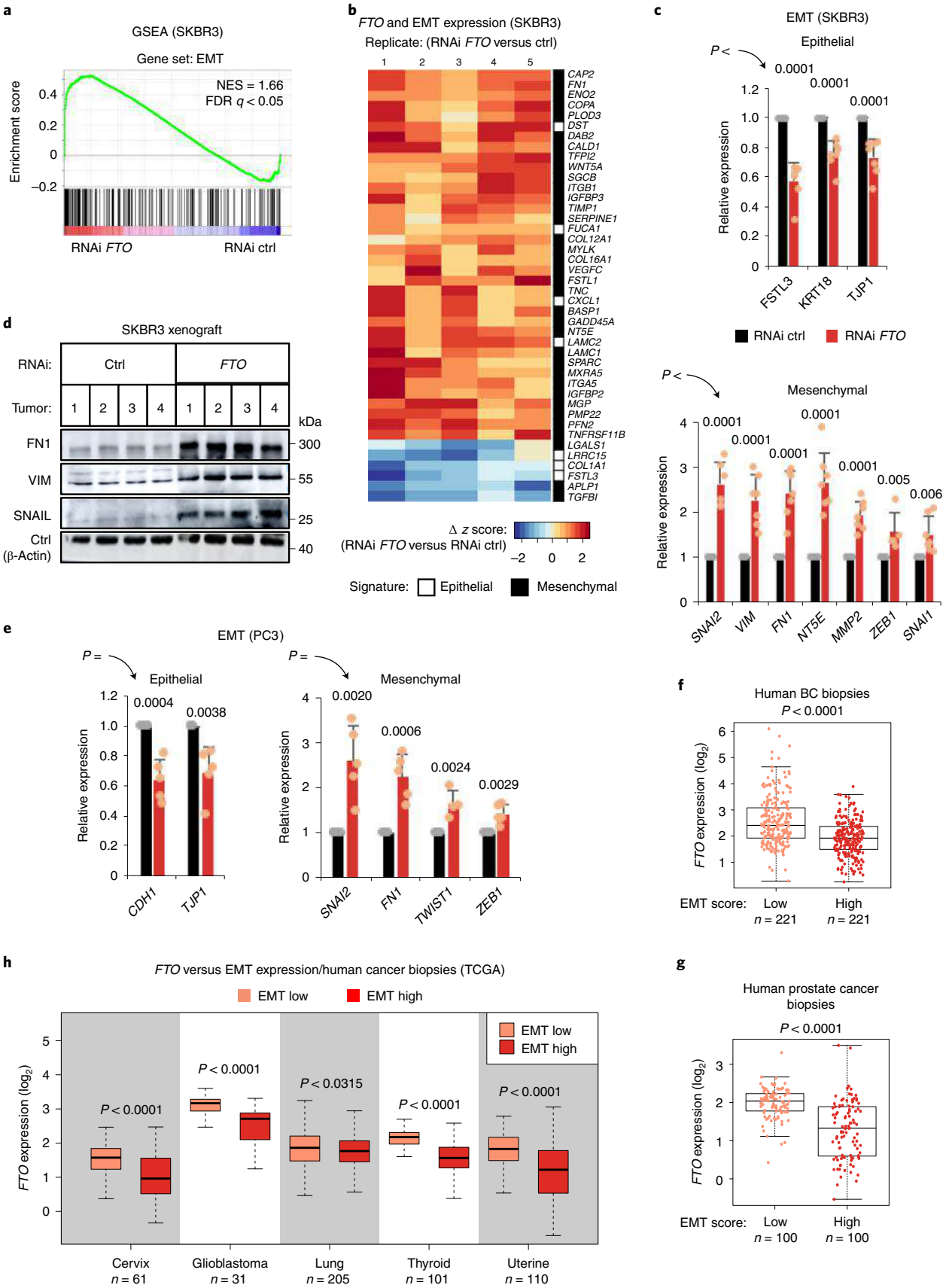

we report *FTO* downregulation in breast cancer. Discrepancies between studies may be due, in part, to limited cohort sizes, particularly in regards to healthy breast tissue, as cohorts of large sizes (that is, TCGA, Oncomine, METABRIC) consistently display *FTO* downregulation and its association with poor prognosis in breast cancer. We further report that loss of *FTO* occurs in all main breast

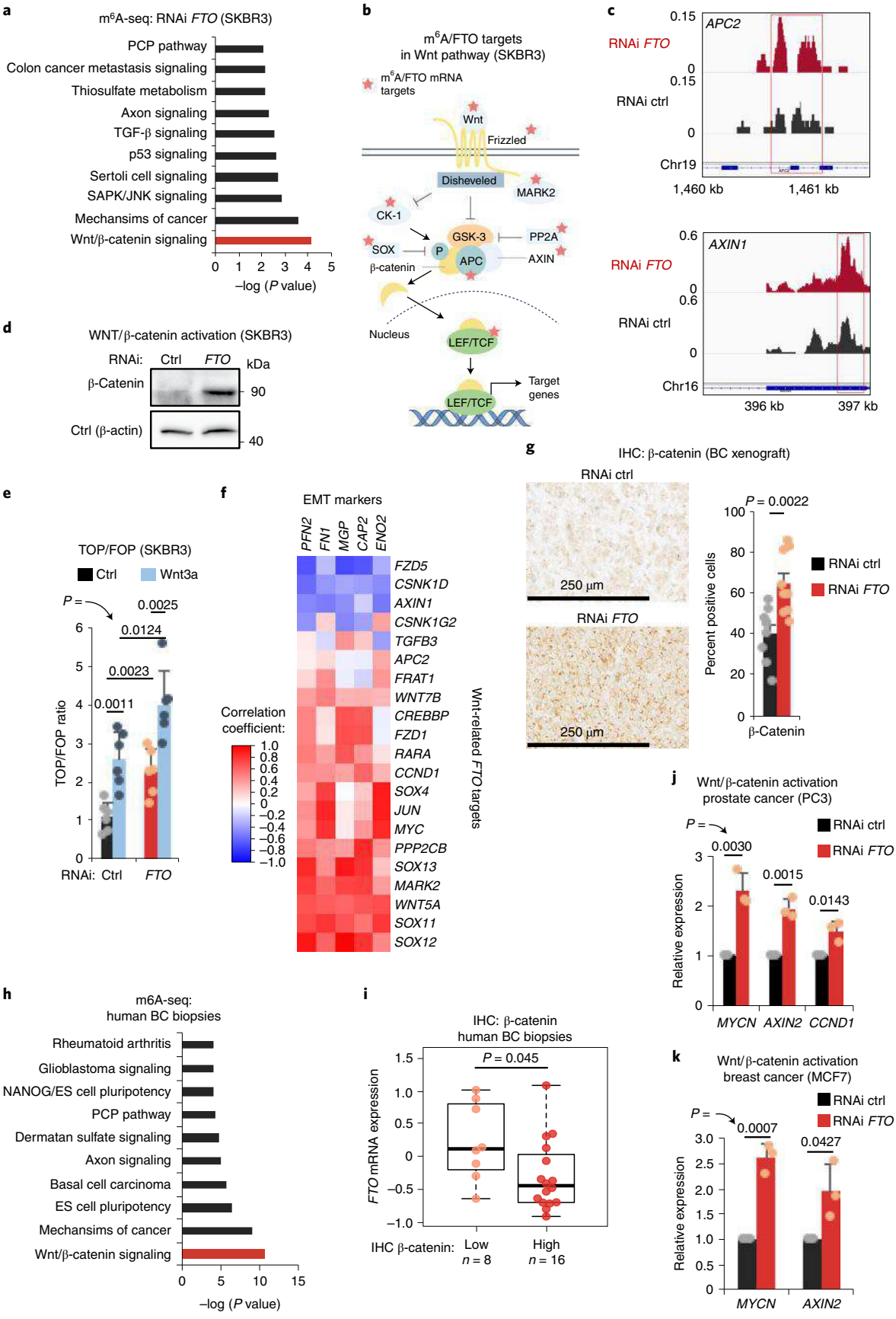

Fig. 5 | FTO controls Wnt signaling in cancer. a, Ingenuity Pathway Analysis (IPA)-performed GO analysis of transcripts that gained m^{6}A following *FTO* depletion in SKBR3 cells. The top ten pathways (by *P* value) are shown. **b**, Schematic representation of m^{6}A/FTO mRNA targets (red asterisks) identified within the Wnt/β-catenin signaling pathway. **c**, Visualization of the immunoprecipitation (IP) m^{6}A signal in RNAi *FTO* and RNAi control SKBR3 cells for *APC2* and *AXIN1* transcripts. **d**, Representative western blot of total β-catenin expression in *FTO*-depleted and control SKBR3 cells ($n=3$). **e**, TOPFlash β-catenin/TCF-LEF reporter assay performed on *FTO* RNAi and control SKBR3 cells (mean + s.d.; $n=6$ per group; *P* values calculated by two-tailed *t*-test as indicated). Wnt3a treatment was used as a positive control for β-catenin-dependent transcriptional activity. **f**, Heat map showing the correlation between the expression of Wnt-related genes identified as FTO targets and representative mesenchymal markers of the EMT hallmark signature (shown in Fig. 4b) measured by RNA-seq in five pairs of SKBR3 cell replicates following *FTO* RNAi. **g**, Immunohistochemistry staining of β-catenin in SKBR3 xenografted tumors (from Fig. 1e at the experiment end point). The percent β-catenin-positive cells is depicted (right; $n=3$ fields × 3 tumors per group; mean + s.e.m.); *P* value calculated by two-tailed *t*-test ($P=0.002$). **h**, GO analysis of m^{6}A-enriched transcripts in human breast cancer biopsies. **i**, Inverse correlation between *FTO* expression and β-catenin signal intensity in human breast cancer biopsies (*n* is the number of tumors; two-tailed Mann–Whitney *U*-test, $P=0.045$). The box defines the IQR split by the median, with whiskers extending to the most extreme values within 1.5 × IQR beyond the box. **j**,**k**, Relative gene expression of Wnt/β-catenin target genes measured by RT-qPCR in PC3 (**j**) or MCF7 (**k**) cells following RNAi of *FTO*; mean + s.d. from three independent experiments normalized to *ACTB* and *SDHA*; *P* values calculated by two-tailed *t*-test as indicated.

cancer subtypes, is widespread among epithelial cancers and promotes Wnt-mediated EMT and tumor progression. Our work not only provides overwhelming evidence for the tumor suppressor function of FTO in epithelial cancers but also highlights the need to better dissect the dual role of FTO in various cancers.

The control of EMT by FTO evidenced here could provide an explanation for the apparent complex roles observed for FTO in tumors. Rather than being a binary process, emerging evidence indicates that EMT occurs through a spectrum of intermediate states and is often only partially reactivated in cancers[45,46]. We propose that dynamic fluctuations of *FTO* levels, according to different tumor types and different stages of progression, may contribute to the context-dependent plastic nature and pleiotropic functions of EMT from cancer initiation to metastasis. Differences in m^{6}A mRNA methylation between tissue types and the versatility of m^{6}A functions further contribute to this complexity, as m^{6}A seems to control EMT in a tissue- and function-specific manner. In cervical cancer, METTL3-mediated m^{6}A methylation at the coding sequence (CDS) of transcripts encoding SNAIL proteins has been shown to trigger protein translation[47]. In breast cancer, we observed increased m^{6}A methylation of the Wnt pathway, a consequence of *FTO* downregulation, as an EMT trigger. This appears to occur through 3′-end processing, a mechanism previously reported for FTO[41]. Changes in 3′-UTR length due to alternative poly(A) site usage affect the binding of microRNAs and RNA-binding proteins, thus affecting transcript stability. This mechanism applies to some Wnt transcripts, and it is likely that the other Wnt-related FTO targets are regulated by a different m^{6}A/FTO-mediated mechanism. Furthermore, we have identified additional signaling pathways as FTO targets in breast cancer (for example, p53 and TGF-β), and future studies could provide insights into their regulation by m^{6}A and their potential cross-talk with Wnt signaling in the context of *FTO* depletion. Collectively, our present work thus reveals that while control of EMT may be a conserved function of m^{6}A in epithelial tumors, it can occur via different mechanisms in different tissues and cancers.

An emerging and intriguing feature of FTO is its association with a variety of distinct signaling pathways. While we have found FTO to negatively control EMT and tumor progression through regulation of transcripts related to Wnt signaling in breast and prostate cancer, in AML, FTO is thought to regulate stem cell differentiation via the ASB2/RARA axis[15]. In melanoma, FTO influences the response to immunotherapy through regulation of cell-intrinsic factors, including PD-1, CXCR4 and SOX10 (ref. [21]). Together this shows that m^{6}A and FTO control a wide variety of cellular processes, and this may further explain the intricate dual nature of FTO in cancers, as some pathways may be more dominant in certain tissues, and thus dysregulation of FTO may lead to different phenotypes. This may be further complicated by the dynamics of the various m^{6}A enzymes and readers and their influence on each other as well as the tissue-specific regulation of FTO activity by post-translational modifications, interaction with other proteins or the presence/absence of cofactors, as shown for epigenetic enzymes with similar functions[48–51]. Lastly, the balance between the tumor-promoting and tumor-suppressing functions of FTO might be influenced by other levels of regulation, such as mutations and changes in key transcription factors, which are highly dependent on the tissue type and even on the subtype of cancer. In breast and prostate cancers, we have found loss of *FTO* to support an EMT program, but in tumors wherein EMT is activated through other means (for example, mutation in the EMT regulators), loss of *FTO* might not favor tumor progression in this way[52]. In conclusion, several molecular mechanisms could shape the activity and distribution of the FTO demethylase and explain discrepancies regarding its functions observed in various cancers.

As previously mentioned, the distribution of m^{6}A is known to be highly tissue specific[4,53]. Accordingly, one would expect FTO also to target different transcripts in different cancer types and subtypes.

Fig. 6 | Wnt signaling is regulated by FTO-dependent m^{6}A demethylation. a, Representative western blot ($n=3$) showing levels of the proteins encoded by two FTO mRNA targets identified within the Wnt/β-catenin signaling pathway (CSNK1D and WNT5A) in RNAi *FTO* and RNAi control SKBR3 cells. HDAC1 and β-actin were used as loading controls. **b**, Volcano plot showing the ROAR score versus the *P* value following depletion of *FTO* in SKBR3 cells. Transcripts with differences in 3′-UTR length ($P<0.05$; paired Fisher test) following knockdown of *FTO* are shown in red (shorter 3′-UTR) and green (longer 3′-UTR). **c**, Gene track view of RNA-seq at *SOX11*, *CSNK1D* and *WNT5A* transcripts displaying significant differences in 3′-UTR length following knockdown of *FTO*. Alternative polyadenylation sites (Poly A) are indicated by vertical yellow lines. Green horizontal lines represent median expression before and after the Poly A site. **d**, Gene expression regulation ($\log_2$ fold change RNAi *FTO*/RNAi control) in SKBR3 cells for FTO targets related to Wnt/β-catenin, p53 and TGF-β (identified in Fig. 4a) measured by RNA-seq in five independent replicates. Transcripts with significant differences in expression ($P<0.05$ by two-tailed *t*-test) are shown in black. Data are shown as $\log_2$ fold change ± lfcSE (standard error of the $\log_2$ fold change); NS, not significant. **e**, Changes in mRNA stability of the FTO targets *WNT5A*, *CSNK1G2* and *CSNK1D* measured by RT-qPCR following transcription inhibition with actinomycin D in SKBR3 cells upon *FTO* knockdown ($n=3$; data relative to 0 h; mean ± s.e.m.).

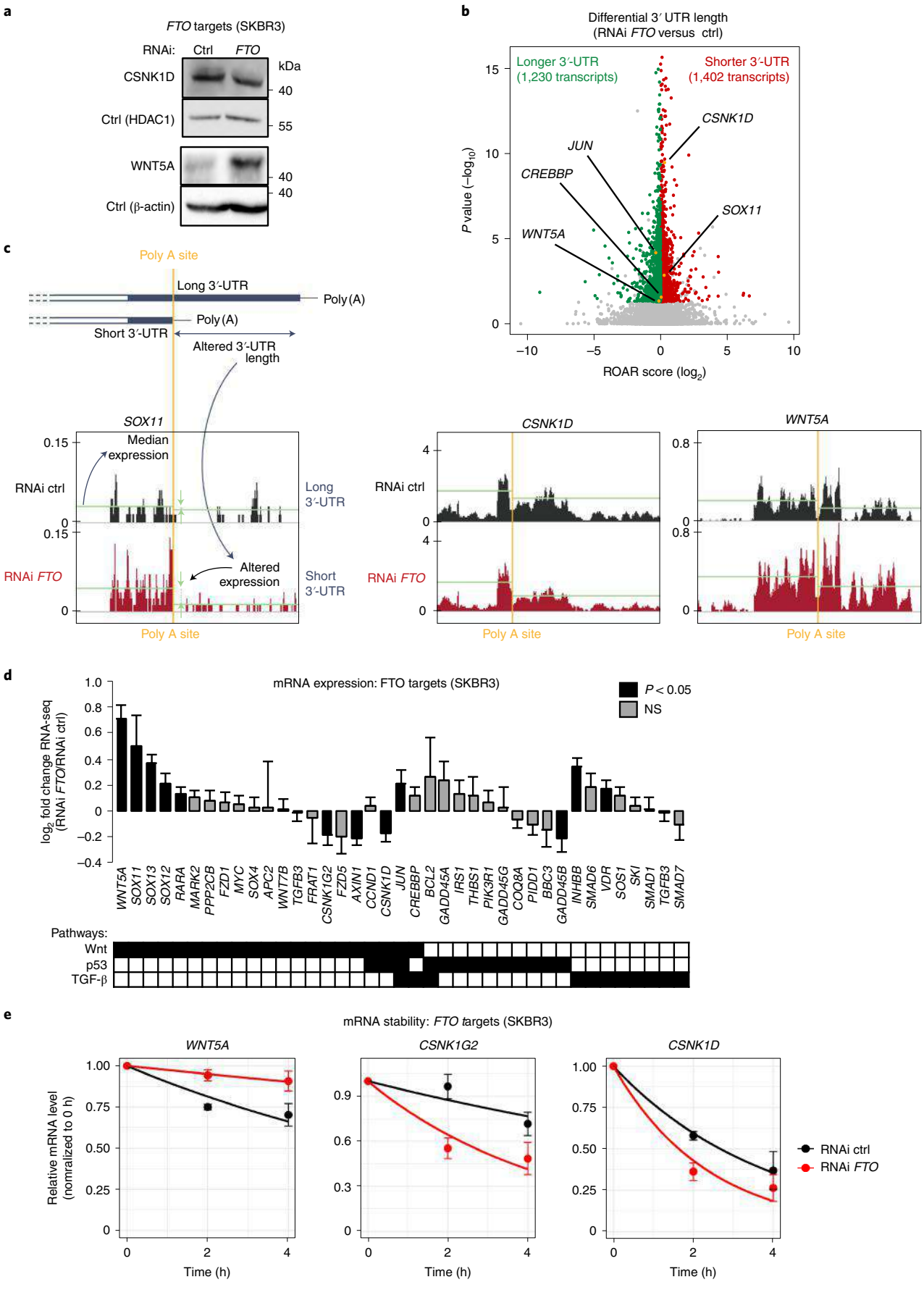
a
FTO targets (SKBR3)
RNAi: Ctrl FTO
kDa
CSNK1D
40
Ctrl (HDAC1)
55
WNT5A
40
Ctrl (β-actin)
40
b
Differential 3′ UTR length
(RNAi FTO versus ctrl)
Longer 3′-UTR
(1,230 transcripts)
Shorter 3′-UTR
(1,402 transcripts)
CSNK1D
JUN
CREBBP
SOX11
WNT5A
P value (−log10)
ROAR score (log2)
c
Poly A site
Long 3′-UTR
Poly (A)
Short 3′-UTR
Poly (A)
Altered 3′-UTR length
SOX11
Median expression
RNAi ctrl
Long 3′-UTR
RNAi FTO
Altered expression
Short 3′-UTR
Poly A site
CSNK1D
RNAi ctrl
RNAi FTO
Poly A site
WNT5A
Poly A site
d
mRNA expression: FTO targets (SKBR3)
P < 0.05
NS
log2 fold change RNA-seq
(RNAi FTO/RNAi ctrl)
WNT5A SOX11 SOX13 SOX12 RARA MARK2 PPP2CB FZD1 MYC SOX4 APC2 WNT7B TGFB3 FRAT1 CSNK1G2 FZD5 AXIN1 CCND1 CSNK1D JUN CREBBP BCL2 GADD45A IRS1 THBS1 PIK3R1 GADD45G COQ8A PIDD1 BBC3 GADD45B INHBB SMAD6 VDR SOS1 SKI SMAD1 TGFB3 SMAD7
Pathways:
Wnt
p53
TGF-β
e
mRNA stability: FTO targets (SKBR3)
WNT5A
CSNK1G2
CSNK1D
Relative mRNA level
(nomralized to 0 h)
Time (h)
RNAi ctrl
RNAi FTO

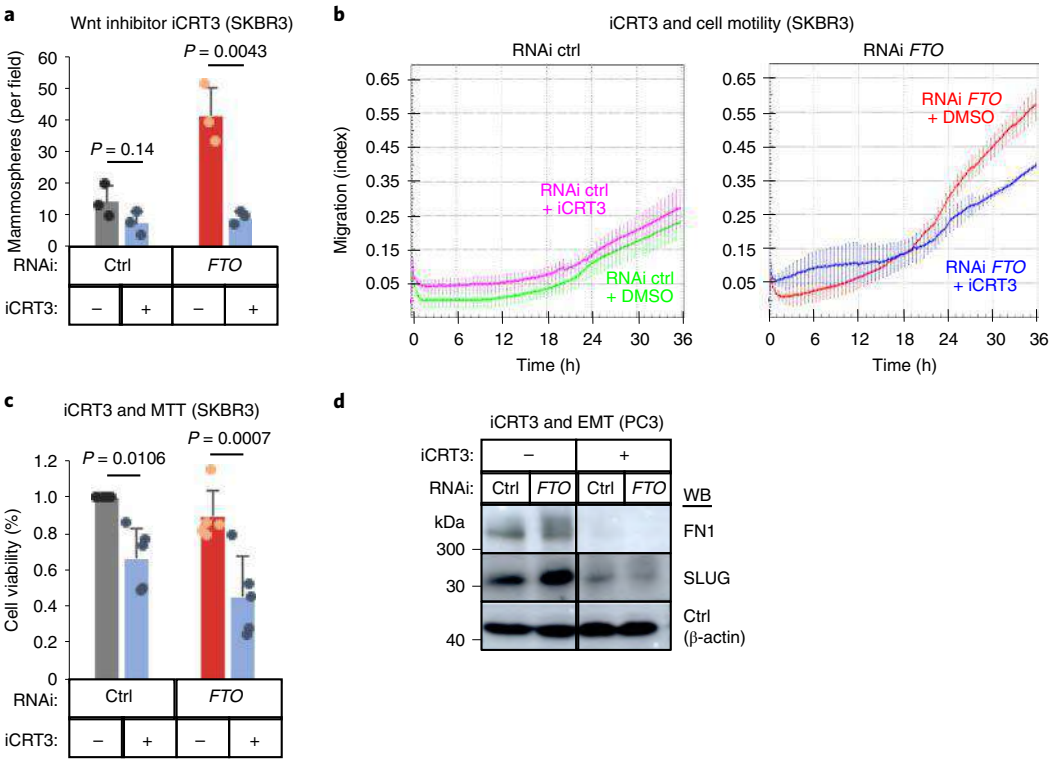

Fig. 7 | In vitro Wnt inhibition restores EMT regulation in *FTO*-depleted cells. a, Effect of Wnt/β-catenin inhibition by iCRT3 pretreatment on mammosphere-forming capacity of RNAi control and RNAi *FTO* SKBR3 cells. Data are from $n = 3$ technical replicates (mean + s.d.) within a single experiment and are representative of three biologically independent experiments provided as source data; *P* values calculated by two-tailed paired *t*-test ($P_{\text{RNAi control}} = 0.14$; $P_{\text{RNAi FTO}} = 0.0043$). **b**, Effect of iCRT3 versus vehicle (DMSO) on the migration capacity of RNAi control and RNAi *FTO* PC3 cells. Data are from $n = 3$ technical replicates (mean + s.d.) within a single experiment and are representative of three biologically independent experiments. Independent repeats have been deposited on the Figshare repository (Figshare, https://doi.org/10.6084/m9.figshare.14788173). **c**, Cell viability following iCRT3 treatment in RNAi control and RNAi *FTO* SKBR3 cells, as measured by MTT assay. Data are shown as mean + s.d.; $n = 5$; *P* values calculated by two-tailed paired *t*-test ($P_{\text{RNAi control}} = 0.01$; $P_{\text{RNAi FTO}} = 0.0007$). **d**, Levels of the mesenchymal EMT marker proteins FN1 and SLUG in RNAi control and RNAi *FTO* PC3 cells in the absence and presence of iCRT3 (representative of three independent replicates), with β-actin used as a loading control.

Indeed, upon mapping m^{6}A in SKBR3 breast cells and PC3 prostate cells, we found only a partial overlap at the transcript level (see Supplementary Tables 2 and 4). But despite this target specificity, FTO appears able to maintain certain functions across tissues. In our study, m^{6}A-seq revealed Wnt signaling as a top dysregulated pathway in both breast and prostate cancers, although the targeted transcripts were partly different. In both models, multiple levels of the Wnt signaling cascade were found to be affected by *FTO* depletion, and increased levels of β-catenin and EMT markers were observed, a finding that was further validated in additional cell lines. Thus, what appears to be conserved is not the identity of affected Wnt-related transcripts but the end point of FTO depletion, EMT activation through β-catenin stabilization. This is not surprising, as it is well documented that the stability of β-catenin is regulated at multiple levels through both positive and negative feedback regulators[54]. Hence, what determines β-catenin stabilization is a combination of effects on FTO targets along this cascade. Importantly, because FTO depletion can either increase or decrease transcript stability[41], the functional impact of FTO on a given transcript cannot be inferred on the sole basis of the presence of an m^{6}A modification. Thus, FTO depletion can be expected to cause Wnt activation by targeting transcripts of both positive and negative feedback regulators along the Wnt pathway. It can promote EMT in different cancer cells by stabilizing β-catenin via different functional impacts on different Wnt-related transcripts. This concept is further supported by our observations with Wnt inhibition; sensitivity to iCRT3, which

Fig. 8 | *FTO*-low tumors are sensitive to Wnt inhibitor therapy. a, Schematic representation of breast cancer xenograft mouse model treated with iCRT3 or DMSO. **b**, Knockdown of *FTO* sensitizes breast tumors to Wnt inhibition. Nude mice growing tumors were treated as indicated in **a** ($n = 5$ tumors per group; mean ± s.e.m.; pictures of representative tumors are shown for each experimental group; two-way ANOVA; $P_{\text{RNAi control}} = 0.0116$, $P_{\text{RNAi FTO}} < 0.0001$). **c**, Tumor metabolism imaging with ^{18}F-FDG PET–CT applied to mice bearing RNAi control or RNAi *FTO*-depleted tumors and treated with or without iCRT3. Representative images are shown for each group (pathological uptake by tumors is circled; physiological uptake in brain (B), kidneys (K), brown fat (F), and muscle (M)). The dotted line represents the lower point of the imaging scale (detection limit). No tumor is circled in the mouse with an iCRT3-treated RNAi *FTO* tumor, as metabolic activity was below the detection limit. Metabolic activity in tumors (middle) and LNs (right) is quantified on the basis of ^{18}F-FDG uptake into SUV_{max}. The box defines the IQR split by the median, with whiskers extending to the most extreme values within 1.5 × IQR beyond the box. The number of samples (*n*) is indicated for each group in parentheses; *P* values calculated by two-tailed *t*-test as indicated. **d**, Nude mice growing tumors from RNAi control (left) or RNAi *FTO* (right) PC3 cells were treated with or without iCRT3 (treatment as indicated in **a** for SKBR3 tumors; $n = 5$ tumors per group; mean ± s.e.m.; pictures of representative tumors are shown for each experimental group; two-way ANOVA; $P_{\text{RNAi control}} > 0.05$, $P_{\text{RNAi FTO}} < 0.0001$).

targets the Wnt signaling cascade below the level of FTO (that is, the TCF/β-catenin complex), is maintained in both breast and prostate cancer cells. This suggests that the effect of the inhibitor depends on the overall effect of FTO depletion and not on a specific set of Wnt transcripts targeted by FTO. In keeping with this reasoning, LGK974, which targets the Wnt pathway above the level of FTO, had no effect in xenografts. Thus, the control of Wnt signaling and EMT by FTO are conserved features in epithelial cancers.

Our study extends far beyond the description of FTO as a tumor suppressor, as the present findings have important clinical

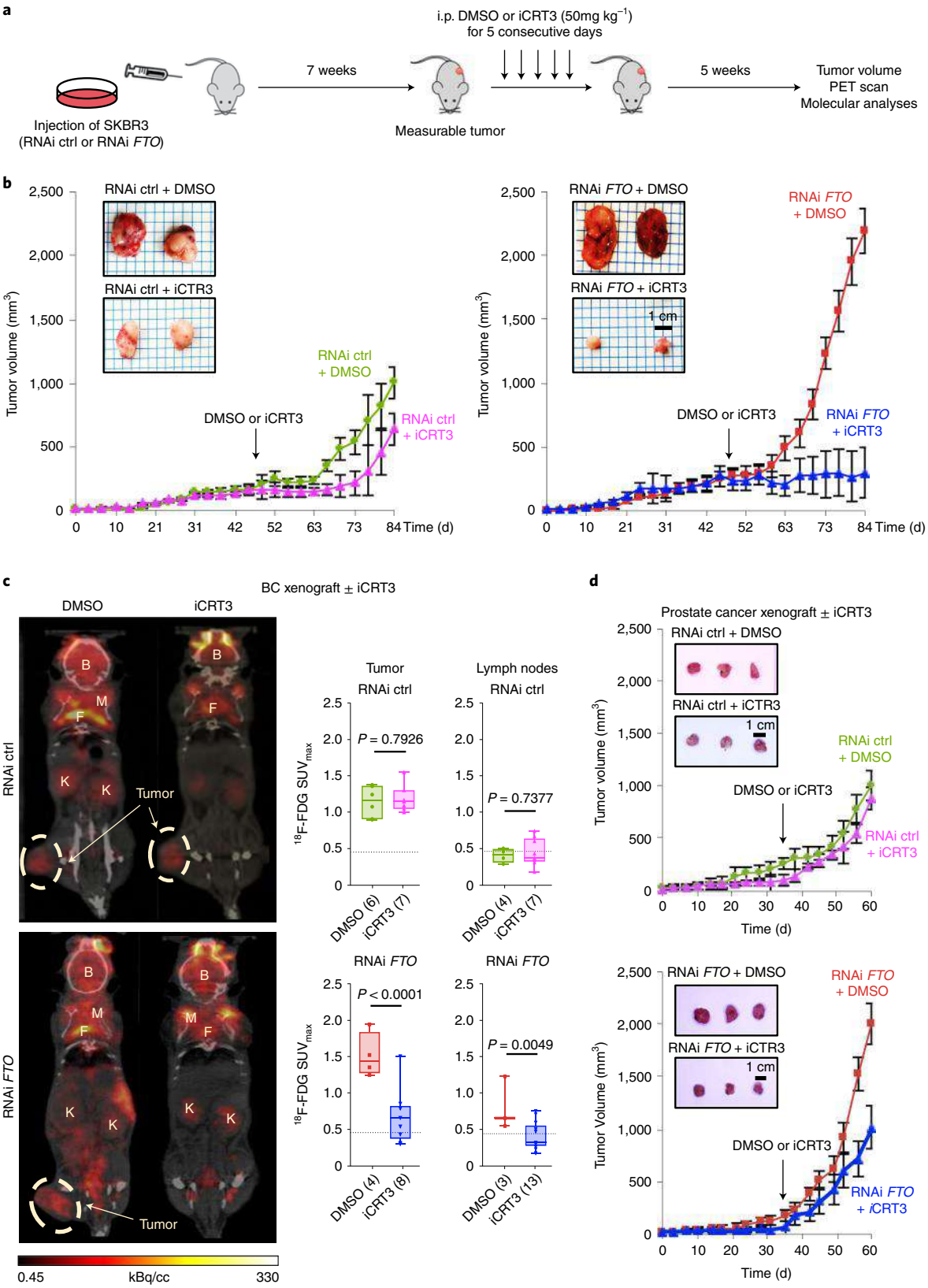

implications. On the one hand, the above considerations regarding the dual role of FTO in cancer should be reckoned with when attempting to develop therapeutic strategies directly targeting the deposition/erasure of the m^{6}A mark. The oncogenic properties of FTO in various cancers have prompted the development of different, more potent inhibitors for the pharmacological targeting of FTO in clinical settings. The results of two recent preclinical studies in AML provided proof-of-concept that targeting FTO may be a valuable anticancer strategy[18,19]. Yet, our results warrant caution in this regard, as we have found pharmacological inhibition of FTO activity in human PDXs to increase the growth of breast tumors. Therefore, this potential therapeutic approach deserves careful consideration, as distinct cancer types and even subtypes are likely to respond differently.

On the other hand, our findings may raise hopes for additional therapeutic strategies. First, despite encouraging evidence from preclinical studies, Wnt signaling inhibitors have not yet progressed beyond phase II due to limited success[55]. However, we demonstrate in our study clear, strong tumor-suppressive effects of Wnt inhibition in an *FTO*-knockdown xenograft model. This key result suggests that the individuals most likely to benefit from Wnt inhibitor treatment, and hence those for whom future trials should be focused, are those with *FTO*-low tumors. A better stratification of individuals, combined with the ongoing development of improved inhibitors[56], may reveal greater sensitivity to Wnt inhibition. Second, from our findings, an alternative clinical implication emerges for the recently developed FTO inhibitors[18,19]. Rather than aiming for single-agent therapy, one might consider combining FTO inhibition with Wnt blockade as a potentially synergistic treatment, regardless of the initial *FTO* status. Opening this avenue could substantially broaden the reach of this application, and this exciting possibility warrants further study.

In conclusion, our work reveals an unexpected mechanistic link between an epigenetic mark on mRNA and key cancer processes. It places the m^{6}A demethylase FTO in a different and surprising light, as a multilevel regulator of Wnt signaling and EMT. The present study tallies with a recent report showing a role for METTL3 in the control of EMT[47]. Our work further indicates that *FTO*-low tumors, although they tend to be more aggressive in many cancer contexts, may carry their own nemesis, sensitivity to Wnt inhibitors. *FTO* level thus emerges as a potential stratifier for Wnt inhibitor treatment and FTO inhibition in combination with Wnt blockade as a potential synergistic anticancer treatment. Hence, our discovery of a previously unrecognized regulatory mechanism linking FTO to Wnt signaling and EMT offers encouraging prospects for cancer research and therapy.

Methods

Human biopsies. Frozen diagnostic samples of individuals with breast cancer admitted to Saint-Louis Hospital (Paris, France) between 2009 and 2013 were obtained from the biological resource center at Saint-Louis Hospital (agreement number DC 2009-929), following the Ethics and Legal National French rules for human information and written consent (ANAES, HAS and INCa).

Human prostate cancer samples were obtained from residual material of a cohort established for a previous study[57]. Samples came from the local tumor tissue bank, C2RC (Lille, France) after approval by the internal review board (CSTMT-042, 27/07/2009). All individuals were informed, and written consent was obtained by the referring physician.

Global m^{6}A quantification. For quantification of m^{6}A in breast and prostate cancers, sample preparation and mass spectrometry analysis was performed as previously described[58]. Nucleosides were analyzed by liquid chromatography–electrospray ionization–tandem mass spectrometry (LC–ESI–MS/MS) using a Shimadzu LC-20AD HPLC system and an AB 3200 QTRAP mass spectrometer (Applied Biosystems) with an electrospray ionization source (Turbo Ionspray). Target nucleosides were monitored in multiple reaction monitoring (MRM) mode, with the following precursor ion → product ion mass transitions: rA (268.1 → 136.1) and m^{6}A (282.1 → 150.1). Within each cohort, FTO levels were measured by RT–qPCR, and samples were divided into two groups ('high' and 'low' expression). The cutoff was determined by the best-performing threshold in terms of the *P* value between both groups (regardless of the direction of the change in m^{6}A), as determined by *t*-test.

For quantification of m^{6}A in matched breast biopsies, nucleoside digestion was performed as previously described[59]. Separation was accomplished by reversed phase chromatography with an Acquity UPLC HSS T3 (Waters) on a VanquishTM Flex Quaternary UHPLC system (Thermo Fisher Scientific). Mass spectrometry was performed on a QuantivaTM triple quadrupole mass spectrometer interfaced with an H-ESI electrospray source (Thermo Fisher Scientific). Data were analyzed with Tracefinder 4.1 (Thermo Fisher Scientific) and Qual browser of Xcalibur 3.0. The mass transitions (precursor → product) for m^{6}A were 282 → 94, 282 → 123 and 282 → 150.

Cell culture and treatments. All cells were cultured at 37 °C under 5% CO_2. SK-BR-3 (abbreviated as SKBR3) and MCF7 cells were cultured in DMEM (Gibco), PC-3c (abbreviated as PC3) cells were cultured in MEM (Gibco) and Ca Ski and H1650 cells were cultured in RPMI (Gibco). All culture media were supplemented with 10% FBS (Gibco) and 1% penicillin and streptomycin (Gibco).

Stable knockdown was done with the pRetroSuper retroviral system (OligoEngine) for *FTO* (1, GTGAAAGGGTCTAATATAA; 2, GACAAAGCCTAACCTACTT) or the scramble control (1, GATCATGTAGATACGCTCA; 2, GAGACCATCACAACCTATT). Replicates of all phenotypic assays were performed with cells generated by two or more independent rounds of infection. All experiments were performed with RNAi *FTO* and control 1, except where RNAi *FTO* and control 2 are indicated.

Overexpression of *FTO* in SKBR3 cells was achieved with the T-Rex systems (Invitrogen). The coding sequence of wild-type *FTO* or of its catalytically inactive mutant (H231A/D233A)[6] was cloned in the pcDNA4/TO vector. Cells were cotransfected with plasmids pcDNA6/TR and pcDNA4/TO. Dual selection was performed with 5 μg ml^{-1} blasticidin (Thermo Fisher Scientific) and 250 μg ml^{-1} zeocin (Invivogen). To induce *FTO* expression, cells were incubated with 2 μg ml^{-1} tetracyclin (Life Technologies) for 24 h.

In rescue experiments, RNAi control and RNAi *FTO* cells were transiently transfected with empty vector (pcDNA3.1+/N-HA) or vector carrying the sequence coding for wild-type or mutant (H231A/D233A) FTO 24 h before the migration assay.

Clonogenicity assays. SKBR3, MCF7, Ca Ski and H1650 cells (2×10^4) and PC3 cells (1×10^4) were seeded in triplicate on pHEMA-coated (Gibco) six-well plates with 2 ml of tumorsphere medium (serum-free DMEM/F12 (Gibco) supplemented with B27 (Gibco) and 20 ng ml^{-1} epidermal growth factor (EGF) (Life Technologies)) and grown for 5–7 d. Spheres were then counted in four fields per well, and the results were averaged. To test for Wnt inhibition, SKBR3 cells were pretreated with either 37.5 μM iCRT3 or vehicle (DMSO) for 24 h before tumorsphere formation.

For colony formation assays, 5×10^3 cells were seeded in triplicate in a six-well plate and grown for 5–10 d in complete medium. Fixation was performed with 10% formaldehyde for 10 min. Cells were then washed twice with water and stained with 0.01% (wt/vol) crystal violet (Sigma-Aldrich) in water for 10 min. After four water washes, plates were dried upside down. Colonies corresponding to at least 50 cells were counted in each well.

Representative examples are shown for tumorsphere and colony formation assays. Data are presented as mean ± s.d. of technical replicates.

Migration and invasion assays. Migration and invasion assays were performed with the Real-Time Cell Analyzer (RTCA) Dual Plate (DP) system (xCELLigence, ACEA Biosciences) and measured by the cell index. For migration assays, 4×10^4 cells were seeded into serum-free medium in the upper chamber of the CIM plates. Quantification was performed by measuring the slope of the curve in the linear phase of migration. For invasion assays, the upper chambers were coated first with 20 μl of Matrigel (BD Biosciences) diluted 1:40 in serum-free medium for 4 h at 37 °C. Then, 6×10^4 SKBR3 or PC3 cells were seeded. The upper chambers were then assembled, with the lower chambers containing medium supplemented with 20% FBS as an attractant, and the system was monitored for 1–2 d. For Wnt inhibition, serum-free medium and Matrigel were supplemented with 37.5 μM iCRT3 (Sigma-Aldrich) or an equal volume of DMSO. For TGF-β treatments, cells were serum-deprived (0.1% FBS) for 24 h before the experiment, and the medium of the lower chamber was either supplemented with 10 ng ml^{-1} TGF-β (R&D Systems) or mock treated.

For scratch assays, cells grown into monolayers were incubated with 1 μg ml^{-1} mitomycin C (Sigma-Aldrich) for 2 h. A wound was generated by scratching the monolayer with a 200-μl pipette tip. Cells were washed once with PBS, and fresh culture medium was added.

Representative examples of at least three independent replicates of migration and invasion assays are shown.

Proliferation and viability assays. Proliferation assays were performed with the RTCA DP system (xCELLigence, ACEA Biosciences) and measured by means of the cell index. SKBR3 cells (10^4) were seeded into RTCA E-Plates and grown for 2 d in complete medium.

The MTT assay kit (Cell Proliferation; Abcam) was used according to the manufacturer's instructions to measure SKBR3 cell viability following iCRT3 treatment (24 h at 37.5 µM).

Mouse xenografts. Female nude (nu/nu) mice of 5–6 weeks of age were inoculated subcutaneously with 10×10^6 cells per flank in 200 µl of 50% Matrigel (Trevigen). For Wnt inhibition, mice were randomized when the tumors reached 200 mm^3 and were injected i.p. daily with vehicle or 50 mg kg^{-1} iCRT3 for 5 consecutive days or given LGK974 (3 mg kg^{-1}) by oral gavage for 14 d. Trastuzumab was injected i.p. (4 mg kg^{-1}) once weekly for 6 weeks. For metastasis assays, cells were resuspended in PBS at 10×10^6 cells per ml, and 0.1 ml was injected into the tail veins of nude mice. The housing temperature for mice was between 20 and 26 °C, with 40–60% humidity and a 14-h light/10-h dark cycle. The experiments were performed in accordance with the European Union Guidelines and were validated by the local Animal Ethics Evaluation Committee (CEBEA protocol number 699N). Values are presented as mean ± s.e.m.

Small-animal PET–CT imaging and analysis. Studies were conducted with a µPET–CT scanner (nanoScan PET/CT, Mediso) on mice injected either subcutaneously or into a tail vein. In subcutaneous xenograft experiments, mice of the control group were scanned twice, once at baseline (4 weeks after inoculation) and once at 9 weeks. Mice of the iCRT3 treatment group were scanned only at the latter time point. In tail vein experiments, mice were scanned 8 or 4 weeks after inoculation. ^{18}F-FDG (4.40 ± 0.32 MBq) was injected into a lateral tail vein, and images were acquired 1 h after injection.

PET–CT image analysis and quantification were performed with PMOD software (PMOD Technologies). Three-dimensional spherical volumes of interest (VOI) were drawn on the PET images of tumor sites or of reference organs selected as probable metastatic sites (that is, lung and liver). A threshold of 40% of the VOI maximum uptake value was applied to assess tracer uptake. Uptake values were normalized to both injected radioactivity and body weight (SUV). The SUV used for the results was the maximum value of the VOI (SUV_{max}). All acquisitions, measurements and analyses were conducted with the experimenters blinded to conditions.

Human-derived xenografts. Experiments on PDXs were performed by Trace, the KU Leuven PDX Platform (Belgium). The PDX model was obtained with informed written participant consent and approval of the UZ Leuven Medical Ethical Committee (S54185). The model was derived from a breast tumor that was positive for the estrogen receptor, negative for the progesterone receptor and low for the HER2/neu receptor. Experiments were carried out in accordance with the principles of the Declaration of Helsinki. PDX experiments had prior approval from the Animal Care and Ethics Committee (project application P038/2015).

Each fresh tumor was rinsed in PBS (Life Technologies) supplemented with penicillin/streptomycin (10,000 IU ml^{-1} penicillin, 1,000 µg ml^{-1} streptomycin; Life Technologies) and amphotericin B (Life Technologies; final concentration 1 µg ml^{-1}). Visible blood clots were removed. The tumor was then cut into small pieces of approximately $3 \times 3 \times 3$ mm^3, and two groups of three pieces each were transferred to two sterile cryotubes containing 500 µl of Matrigel (BD Biosciences). FTO inhibitor MA (Sigma-Aldrich; 0.25 mg kg^{-1})[30] or water was then added to the Matrigel in the cryovials. The cryotubes were kept on ice for 3 h before subcutaneous implantation into the interscapular fat pad of anesthetized female NMRI nude mice (minimum 6 weeks old; Taconic) through a small incision in the skin of the back. Tumors were treated both before and after implantation, because after implantation, MA treatment alone did not yield any difference in tumor size (data not shown). The incision was closed with a sterile suture clip, and analgesia (buprenorphine) was delivered postoperatively. Mice xenografted with MA-pretreated tumors also received MA throughout engraftment (0.25 mg kg^{-1} in water, intratumoral injection weekly for 4 weeks); the other mice were treated with water. Body weight and tumor volume were measured every other day. The mice were killed when the tumor reached 2,000 mm^3 or if the mice showed clear signs of distress. Xenografts were collected, measured and processed for further analyses (fresh frozen and formalin fixed). Values are presented as means ± s.e.m.

Association between FTO expression and phenotypic/clinical features in cancer. Associations between the *FTO* mRNA level and either distant metastasis-free survival, relapse-free survival or overall survival were evaluated with the Cox proportional hazards regression model, using the Kaplan–Meier plotter website (http://kmplot.com/analysis)[60] for breast (cohort referred to as the KM cohort), lung and uterine cancers. METABRIC data and TCGA data were also used for breast and prostate cancer, respectively. Statistical significance was assessed by logrank test. In the cohorts from the Kaplan–Meier website and METABRIC, *FTO*-high and *FTO*-low groups were generated on the basis of a trichotomized cutoff. For TCGA prostate cancers, samples with the 40% highest and 40% lowest *FTO* expression were classified as *FTO*-high and *FTO*-low groups, respectively. For breast cancer, cohorts analyzed as an aggregate through the Kaplan–Meier plotter website were also tested individually to evaluate the variation between cohorts. Given the smaller size of the individual cohorts, the expression cutoff between *FTO*-high and *FTO*-low groups was determined by the best-performing threshold in terms of the *P* value (determined by logrank test) between the two groups in each cohort, regardless of the direction of the hazard ratio.

Associations in breast cancer between the *FTO* mRNA level and clinical features (tumor grade or LN invasion) were evaluated in the METABRIC cohort[61]. Node invasion information was binarized into two categories: 'no LN invasion' (negative) and 'at least one node invaded' (positive). As the Shapiro–Wilk test indicated that the values were not normally distributed, non-parametric tests were used, that is, the Kruskal–Wallis test for tumor grade and the Wilcoxon test for node positivity.

The association between the *FTO* transcript level and tumor progression in prostate cancer was evaluated in the dataset GSE3325 (ref. [62]). One-way ANOVA without equality of variance and the Kruskal–Wallis test were used to measure statistical significance.

For the association between the *FTO* transcript level and the EMT signature, 'TCGA-BRCA' and 'TCGA-PRAD' RNA-seq data (as FPKM values) were used. A metagene for EMT was generated on the basis of the signature from Rokavec et al.[63]. For each gene of the EMT signature, we centered the mean at 0 and scaled individual values by the gene standard deviation to normalize the variance of all genes. The expression value of each gene for the 'Epithelial state' was multiplied by −1, with 'Mesenchymal state' genes unchanged. For each sample, the metagene value of EMT was computed as the mean of all scaled gene expression values in Rokavec's signature. The samples were then stratified between 'EMT-low' (samples showing the 20% lowest values for the EMT metagene) and 'EMT-high' (20% highest), and a *t*-test was used to evaluate the significance of changes in *FTO* expression.

RNA extraction and RT–qPCR. Total RNA was extracted with the RNeasy Kit (Qiagen). For grafted tissue, frozen samples were first homogenized using the FastPrep-24 homogenizer system with lysing matrix D (MP Biomedicals) in RLT buffer supplemented with β-mercaptoethanol. Removal of residual DNA was performed with the RNase-Free DNase set (Qiagen). One microgram of total RNA was reverse transcribed with the First Strand cDNA Synthesis kit (Roche). Real-time PCR was performed with the LightCycler 480 Probes Master kit (Roche).

Primer sequences are listed in Supplementary Table 5. Gene expression was normalized by the $2^{-\Delta\Delta C_t}$ method, with *ACTB* and *SDHA* as reference genes. Values are presented as mean ± s.d. of $n \geq 3$ independent replicates as indicated.

For Wnt inhibition, cells were treated with 37.5 µM iCRT3 for 12 h before cell collection. For EMT induction, cells were treated with 10 ng ml^{-1} TGF-β for 6 h before cell collection. In mRNA stability assays, cells were treated with 5 µg ml^{-1} actinomycin D (Sigma-Aldrich) for 0, 2, 4 or 6 h before cell collection. *GAPDH*, a highly stable transcript, was chosen as the reference gene for all stability assays. After RT–qPCR, expression values (relative to 0 h) were fitted to an exponential decay model using R.

Paired-end RNA-seq. Library preparation was performed from total RNA with TruSeq Stranded Total RNA Library Prep Gold (Illumina) and TruSeq RNA Single Indexes (Illumina) according to the manufacturer's instructions. Reads were filtered against low-complexity and adapter content using AfterQC (default parameters)[64] and Trimmomatic (ILLUMINACLIP:2:30:10, LEADING:3, TRAILING:3)[65] and mapped using STAR (hg19 genome, Ensembl transcriptome version 85)[66]. Differentially expressed genes were identified using a DeSeq2 paired analysis after read counting with the HTSeq count tool[67,68]. For GSEA[69], the 'signed' significance (that is $-\log_{10}$ of the differential *P* value multiplied by −1 for genes downregulated in RNAi *FTO*) was used to rank each gene. This ranked list was submitted to GSEA to identify enriched hallmark gene sets from MSigDB (http://software.broadinstitute.org/gsea/msigdb/). For alternative poly(A) site usage, mapped reads were submitted to the ROAR algorithm via the 'roarWrapper_chrBychr.R' script (https://github.com/vodkatad/roar/blob/master/inst/examples/) using the human poly(A) sites from polyADB_v2 (ref. [70]).

Western blotting. For cultured cells, 50 µg of whole-cell extract was loaded and electrophoresed on 8% SDS–polyacrylamide gels, transferred onto a PVDF membrane (PerkinElmer) and subjected to western blot analysis. Antibodies were diluted in 5% (wt/vol) nonfat dry milk in PBS containing 0.1% Tween-20 (Supplementary Table 5). Western blots were visualized with the ECL Plus system (Amersham Biosciences).

For nuclear and cytoplasmic protein extraction, cells were lysed in cytoplasm lysis buffer (50 mM Tris-HCl pH 7.4., 10 mM NaCl, 0.5% NP-40 and 0.25% Triton X-100 supplemented with cOmplete Mini Protease Inhibitor Cocktail) for 15 min on ice. After centrifuging for 10 min at 3,500*g*, the supernatant was kept as cytoplasmic extract. Pellets were washed five times in cytoplasm lysis buffer without NP-40 (centrifuging for 5 min at 3,500*g* in between), diluted in 2× Laemmli buffer and used as nuclear extracts.

For grafted tissues, frozen samples were first homogenized with the FastPrep-24 homogenizer system with M-PER (Thermo Fischer Scientific) lysis buffer (0.1 g ml^{-1}) supplemented with Protease Inhibitor Cocktail EDTA-free (Thermo Fischer Scientific) and Phosphatase Inhibitor Cocktail (Thermo Fischer Scientific). Western blots were visualized with the SuperSignal West Pico Chemiluminescent Substrate (Pierce).

Full scans of all the blots are available as Source Data.

m^{6}A-seq. The method for m^{6}A-seq was adapted from a protocol described previously[3]. Total RNA was fragmented using a fragmentation buffer (final concentration 10 mM Tris-HCl and 10 mM $ZnCl_2$) and incubating at 94 °C for 35 s. Then, one-tenth volume of 0.5 M EDTA was added, and the tubes were placed on ice. RNA was then subjected to sodium acetate precipitation and resuspended in RNase-free water. Fragmentation size was assessed by a 2100 Bioanalyzer (Agilent). Then, 2–5 µg of fragmented RNA was kept at −80 °C to serve as input. The RNA was denatured by heating (70 °C for 5 min then placed on ice), and the IP mix was prepared as follows: 250 µg of fragmented RNA from cultured cells or 100 µg of fragmented RNA from human breast cancer biopsies ajusted to a volume of 755 µl with water, 10 µl (400 U) of RNasin Ribonuclease Inhibitors (Promega), 10 µl of 200 mM Ribonucleoside Vanadyl Complex (RVC; NEB), 200 µl of IP buffer 5× (50 mM Tris-HCl, 750 mM NaCl, 0.5% (vol/vol) Igepal), 7.8 µl of anti-m^{6}A antibody (Synaptic System 202003) and 17.2 µl of RNase-free water. The mix was incubated overnight at 4 °C on a rotation wheel. The next day, 60 µl of G protein dynabeads (Invitrogen, 10004D) was washed twice with 1× IP buffer supplemented with antiproteases (Roche) and blocked by incubating the beads in wash buffer supplemented with 0.5 mg ml^{-1} BSA for 1 h on a rotation wheel. The beads were washed again twice, added to the IP mix and incubated for 2 h at 4 °C on a rotation wheel. The beads were washed three times with 1 ml of washing buffer supplemented with 10 µl of RNasin and 10 µl of RVC. Elution was performed by TriPure (Roche) extraction, and RNA was resuspended in 13 µl of RNase-free water. Reverse transcription of 11 µl of immunoprecipitated RNA was done with the SuperScript II Reverse Transcriptase kit (Invitrogen) according to the manufacturer's instructions. Second-strand synthesis was performed from cDNA with the NEBNext mRNA Second Strand Synthesis Module (NEB), according to the manufacturer's instructions. Double-stranded DNA was purified by MinElute PCR purification (Qiagen) and quantified by Qubit (Thermo Fisher Scientific). A sequence library was prepared with a MicroPlex Library Preparation Kit v2 ×12 (Diagenode) for both input and IP samples, which were then sequenced with an Illumina NextSeq500. For SKBR3 RNAi *FTO* and control cells, two replicates (from independent infections) were sequenced.

Bioinformatic analysis of m^{6}A-seq data. Reads were mapped using STAR[66] (hg19 genome, RefSeq transcriptome downloaded in 2012). Peaks (m^{6}A-enriched regions) and differential peaks were identified using the script available on GitHub (https://github.com/martinBizet/m6A_FTO_cancer). Briefly, we used MACS2 to define peaks (using IP samples and their input counterpart as controls) and 'expected peaks' (using input as an IP and no control) ($q < 0.05$)[71]. The 'expected genome size' MACS2 parameter was set as the sum of exon and intron lengths (counting only once regions that were shared by several transcripts). To avoid extremely large m^{6}A-enriched regions, the peaks were then resized to 100 base pairs (bp) on both sides of the summit. Then, both peaks and expected peaks were annotated (5′-UTR, CDS, 3′-UTR or intronic) by intersecting peak center positions with RefSeq annotations. Peaks remaining unannotated were defined as 'intergenic'. Peaks associated with more than one region were categorized as 'multiple'. m^{6}A enrichment of each annotation region was evaluated as the ratio between the percentages of m^{6}A peaks and expected peaks in this region. For differential analyses between two conditions, each replicate experiment was analyzed separately by comparing enrichment ratios computed using the following procedure. Positions of the peaks from the two conditions were first merged (using bedtools merge)[72] to obtain peaks identified in at least one condition. Bedgraph files, generated from the mapped reads, were used to measure the coverage at each merged peak position. To correct for mapping and transcription biases, the enrichment ratio was defined for each peak for each condition as the ratio of the peak transcripts per million (TPM) for IP over the maximum of the peak or gene TPM of input. GO was performed with IPA (Qiagen).

Motif analysis. The strand of each m^{6}A and expected peak was attributed by associating it to its RefSeq transcript using 'bedtools intersect'[72] (intergenic peaks were ignored, and peaks associated to both strands were duplicated). Sequences were extended to 250 bp on each side of the peak center, and the 2,500 peaks with the highest MACS2 fold enrichment were extracted by strand using 'bedtools getfasta'[72]. The Meme-suite tools (http://meme-suite.org)[73] were then used; 'Ame' was used to evaluate the enrichment significance of the 'DRACH' motif using a first-order Markov model generated using the 'fasta-get-markov' on input sample sequences as a background model and expected peaks as negative control peaks. The scoring method was 'avg', and the test method was 'ranksum'. 'Meme-chip' (DREME and MEME) was used to confirm the presence of 'DRACH'-like sequences among the top overrepresented motifs using the same background model and negative peaks as 'Ame'. The numbers of DREME and MEME motifs were restricted to 10, and the MEME-searching windows were set between 5 and 12.

TOPFlash/FOPFlash reporter assay. The vectors Super 8× TOPFlash (plasmid 12456; a firefly luciferase reporter of β-catenin-mediated transcriptional activation) and Super 8× FOPFlash (plasmid 12457; a negative mutant control) were purchased from Addgene[74]. SKBR3 cells were grown to 80% confluency in a six-well plate, and TransIT-LT1 Transfection Reagent (Mirus Bio) was used to cotransfect cells with 1.5 µg of TOP or FOP plasmid and 300 ng of a vector coding for the *Renilla* luciferase (used as an internal control for transfection efficiency and other potential confounding sources of variation). After 2 d, the cells were subjected to mock treatment or 100 ng ml^{-1} Wnt3a (Abcam) or iCRT3 (Sigma-Aldrich) at doses of 1.5, 7.5 or 37.5 µM for 24 h. Luciferase activity was measured with the Dual-Glo Luciferase Assay System (Promega). Firefly luciferase was first normalized to the *Renilla* control signal, then the TOP/FOP ratio was calculated. Values are presented as mean ± s.d. of $n \geq 3$ independent replicates.

IHC. IHC data on β-catenin levels in human biopsies were obtained previously as part of a series of centrally reviewed breast cancer cases[40], with matching microarray data deposited as GSE88770 in the Gene Expression Omnibus (GEO) database for *FTO* gene expression[75]. The probe level intensities were background adjusted by the robust multiarray analysis method followed by quantile normalization so that the 2.5% and 97.5% quantiles equaled −1 and +1, respectively. The β-catenin IHC data are provided in Supplementary Table 6. The Mann–Whitney *U*-test was used to evaluate the significance of changes in *FTO* expression between groups showing low and high β-catenin levels.

In xenograft and PDX experiments, formalin-fixed, paraffin-embedded tissue sections (4 µm) were immunohistochemically stained (antibodies are listed in Supplementary Table 5). IHC staining was performed with the Mouse on Mouse Polymer IHC kit (Abcam) on a Ventana Benchmark XT automated staining instrument (Ventana Medical Systems) for mouse antibodies and manually with the SignalStain Boost IHC Detection Reagent (Cell Signaling Technology) for rabbit antibodies. Three regions were selected at random on different parts of the section (three xenografts per condition) and analyzed with the QuPath program.

For immunofluorescence staining of β-catenin, cells grown on coverslips were washed three times, covered with ice-cold acetone and incubated for 10 min at −20 °C. After three washes with PBS, slides were incubated with blocking buffer (1% BSA in PBS) for 1 h at room temperature. After removal of PBS, the primary antibody was added to each slide and incubated overnight at 4 °C. Slides were washed three times with PBS and incubated with the secondary antibody for 2 h at room temperature protected from light. After three additional washes, excess PBS was removed, and coverslips were mounted on slides with ProLong with DAPI (Life Technologies).

Statistics and reproducibility. Data are presented as means ± s.e.m. or means ± s.d. as indicated. When box plots are used to visualize data distributions, center lines show medians, box limits are upper and lower quartiles and whiskers represent 1.5 × IQR. A two-tailed Student's *t*-test or one-way ANOVA was used when normal distribution (evaluated by Shapiro–Wilk test) could be assumed, and Wilcoxon or Kruskal–Wallis tests were used otherwise. Effect size was estimated using Cohen's *d* distance. For PDX, differences in tumor volume among groups of mice were tested using a mixed effects model, as implemented in GraphPad Prism, which uses a compound symmetry covariance matrix and is fit using restricted maximum likelihood. All replicates for in vitro data are derived from independent experiments (with multiple RNAi infections), except for clonogenicity assays for which a representative result (with technical replicates) is shown (with independent experiments presented in the Source Data). Graphs for Figs. 2a,b, 3c,e and 7b and Extended Data Figs. 2a,b,d,e, 3c,f and 4d were generated by xCELLigence and downloaded directly from the machine, so numerical source data are not available. All independent repeats that support the findings of these experiments are available on the Figshare repository (https://doi.org/10.6084/m9.figshare.14602932, https://doi.org/10.6084/m9.figshare.14602944, https://doi.org/10.6084/m9.figshare.14788173, https://doi.org/10.6084/m9.figshare.14602965, https://doi.org/10.6084/m9.figshare.14602971 and https://doi.org/10.6084/m9.figshare.14602986). All replicates for in vivo mouse data and human biopsies are from different tumors. No statistical method was used to predetermine sample size. No data were excluded from the analyses. Experiments using cultured cells and mice were randomized. Blinding was exclusively used for PET imaging analyses.

Further information on research design is available in the Nature Research Reporting Summary linked to this article.

Reporting Summary. Further information on research design is available in the Nature Research Reporting Summary linked to this article.

Data availability

Sequencing data that support the findings of this study have been deposited in the GEO repository under accession number GSE128582. Human cancer data (bladder urothelial carcinoma, breast invasive carcinoma, cervical squamous cell carcinoma and endocervical adenocarcinoma, glioblastoma multiforme, kidney chromophobe, lung adenocarcinoma and lung squamous cell carcinoma, prostate adenocarcinoma, thyroid carcinoma and uterine corpus endometrial carcinoma) were derived from the TCGA Research Network (http://cancergenome.nih.gov/). RNA-seq data from TCGA were obtained as normalized FPKM counts from GDC (https://portal.gdc.cancer.gov/repository), and PAM50 subtype information was extracted from UCSC Xena (https://xenabrowser.net). METABRIC expression

and clinical data[61] were downloaded through the European Genome-Phenome Archive (EGA) (http://www.ebi.ac.uk/ega/, accession number EGAS00000000083). Previously published microarray data that were reanalyzed here are available under accession codes GSE9195, GSE10780, GSE10810, GSE12276, GSE19615, GSE20711 and GSE21653. Reannotation and processing of Affymetrix Human Genome U133 Plus 2.0 array data were performed as previously detailed[76].

The hg19 reference transcriptome (version 85) was obtained from the Ensembl portal (ensembl.org). Hallmark gene sets were obtained from the MsigDB database (https://www.gsea-msigdb.org/gsea/msigdb). Human poly(A) sites were obtained from PolyA_DB2 (http://polya.umdnj.edu/PolyA_DB2).

For motility assays related to Figs. 2a,b, 3c,e and 7b and Extended Data Figs. 2a,b,d,e, 3c,f and 4d, independent repeats have been deposited on the Figshare repository (https://doi.org/10.6084/m9.figshare.14602932, https://doi.org/10.6084/m9.figshare.14602944, https://doi.org/10.6084/m9.figshare.14602953, https://doi.org/10.6084/m9.figshare.14602965, https://doi.org/10.6084/m9.figshare.14602971 and https://doi.org/10.6084/m9.figshare.14602986). Source data are provided with this paper. All other data supporting the findings of this study are available from the corresponding author on reasonable request.

Code availability

Code supporting this study is available at a dedicated GitHub repository (https://github.com/martinBizet/m6A_FTO_cancer).

Received: 12 June 2019; Accepted: 17 May 2021;
Published online: 23 June 2021

References

1. Harcourt, E. M., Kietrys, A. M. & Kool, E. T. Chemical and structural effects of base modifications in messenger RNA. *Nature* **541**, 339–346 (2017).
2. Boccaletto, P. et al. MODOMICS: a database of RNA modification pathways. 2017 update. *Nucleic Acids Res.* **46**, D303–D307 (2018).
3. Dominissini, D. et al. Topology of the human and mouse m^{6}A RNA methylomes revealed by m^{6}A-seq. *Nature* **485**, 201–206 (2012).
4. Meyer, K. D. et al. Comprehensive analysis of mRNA methylation reveals enrichment in 3′ UTRs and near stop codons. *Cell* **149**, 1635–1646 (2012).
5. Shi, H., Wei, J. & He, C. Where, when, and how: context-dependent functions of RNA methylation writers, readers, and erasers. *Mol. Cell* **74**, 640–650 (2019).
6. Jia, G. et al. N^6-methyladenosine in nuclear RNA is a major substrate of the obesity-associated FTO. *Nat. Chem. Biol.* **7**, 885–887 (2011).
7. Zheng, G. et al. ALKBH5 is a mammalian RNA demethylase that impacts RNA metabolism and mouse fertility. *Mol. Cell* **49**, 18–29 (2013).
8. Deng, X., Su, R., Stanford, S. & Chen, J. Critical enzymatic functions of FTO in obesity and cancer. *Front. Endocrinol.* **9**, 396 (2018).
9. Geula, S. et al. Stem cells. m^{6}A mRNA methylation facilitates resolution of naïve pluripotency toward differentiation. *Science* **347**, 1002–1006 (2015).
10. Meyer, K. D. et al. 5′ UTR m^{6}A promotes cap-independent translation. *Cell* **163**, 999–1010 (2015).
11. Zhou, J. et al. Dynamic m^{6}A mRNA methylation directs translational control of heat shock response. *Nature* **526**, 591–594 (2015).
12. Liu, N. et al. N^6-methyladenosine-dependent RNA structural switches regulate RNA–protein interactions. *Nature* **518**, 560–564 (2015).
13. Yue, Y., Liu, J. & He, C. RNA N^6-methyladenosine methylation in post-transcriptional gene expression regulation. *Genes Dev.* **29**, 1343–1355 (2015).
14. Fu, Y., Dominissini, D., Rechavi, G. & He, C. Gene expression regulation mediated through reversible m^{6}A RNA methylation. *Nat. Rev. Genet.* **15**, 293–306 (2014).
15. Li, Z. et al. FTO plays an oncogenic role in acute myeloid leukemia as a N^6-methyladenosine RNA demethylase. *Cancer Cell* **31**, 127–141 (2017).
16. Su, R. et al. R-2HG exhibits anti-tumor activity by targeting FTO/m^{6}A/MYC/CEBPA signaling. *Cell* **172**, 90–105 (2018).
17. Vu, L. P. et al. The N^6-methyladenosine (m^{6}A)-forming enzyme METTL3 controls myeloid differentiation of normal hematopoietic and leukemia cells. *Nat. Med.* **23**, 1369–1376 (2017).
18. Huang, Y. et al. Small-molecule targeting of oncogenic FTO demethylase in acute myeloid leukemia. *Cancer Cell* **35**, 677–691 (2019).
19. Su, R. et al. Targeting FTO suppresses cancer stem cell maintenance and immune evasion. *Cancer Cell* **38**, 79–96 (2020).
20. Cui, Q. et al. m^{6}A RNA methylation regulates the self-renewal and tumorigenesis of glioblastoma stem cells. *Cell Rep.* **18**, 2622–2634 (2017).
21. Yang, S. et al. m^{6}A mRNA demethylase FTO regulates melanoma tumorigenicity and response to anti-PD-1 blockade. *Nat. Commun.* **10**, 2782 (2019).
22. Zhuang, C. et al. N^6-methyladenosine demethylase FTO suppresses clear cell renal cell carcinoma through a novel FTO–PGC-1α signalling axis. *J. Cell. Mol. Med.* **23**, 2163–2173 (2019).
23. Rong, Z. X. et al. Downregulation of fat mass and obesity associated (FTO) promotes the progression of intrahepatic cholangiocarcinoma. *Front. Oncol.* **9**, 369 (2019).
24. Wen, L., Pan, X., Yu, Y. & Yang, B. Down-regulation of FTO promotes proliferation and migration, and protects bladder cancer cells from cisplatin-induced cytotoxicity. *BMC Urol.* **20**, 39 (2020).
25. Niu, Y. et al. RNA N^6-methyladenosine demethylase FTO promotes breast tumor progression through inhibiting BNIP3. *Mol. Cancer* **18**, 46 (2019).
26. Wu, L., Wu, D., Ning, J., Liu, W. & Zhang, D. Changes of N^6-methyladenosine modulators promote breast cancer progression. *BMC Cancer* **19**, 326 (2019).
27. Xu, Y. et al. The FTO/miR-181b-3p/ARL5B signaling pathway regulates cell migration and invasion in breast cancer. *Cancer Commun.* **40**, 484–500 (2020).
28. Peitzsch, C., Tyutyunnykova, A., Pantel, K. & Dubrovska, A. Cancer stem cells: the root of tumor recurrence and metastases. *Semin. Cancer Biol.* **44**, 10–24 (2017).
29. Moro, M. et al. Establishment of patient derived xenografts as functional testing of lung cancer aggressiveness. *Sci. Rep.* **7**, 6689 (2017).
30. Huang, Y. et al. Meclofenamic acid selectively inhibits FTO demethylation of m^{6}A over ALKBH5. *Nucleic Acids Res.* **43**, 373–384 (2015).
31. Gil-Rendo, A. et al. Association between [18F]fluorodeoxyglucose uptake and prognostic parameters in breast cancer. *Br. J. Surg.* **96**, 166–170 (2009).
32. Groheux, D., Espié, M., Giacchetti, S. & Hindié, E. Performance of FDG PET/CT in the clinical management of breast cancer. *Radiology* **266**, 388–405 (2012).
33. Angeloni, V., Tiberio, P., Appierto, V. & Daidone, M. G. Implications of stemness-related signaling pathways in breast cancer response to therapy. *Semin. Cancer Biol.* **31**, 43–51 (2015).
34. Velloso, F. J. et al. The crossroads of breast cancer progression: insights into the modulation of major signaling pathways. *Onco. Targets Ther.* **10**, 5491–5524 (2017).
35. Zhou, S. et al. FTO regulates the chemo-radiotherapy resistance of cervical squamous cell carcinoma (CSCC) by targeting β-catenin through mRNA demethylation. *Mol. Carcinog.* **57**, 590–597 (2018).
36. Hu, B. et al. Epigenetic activation of WNT5A drives glioblastoma stem cell differentiation and invasive growth. *Cell* **167**, 1281–1295 (2016).
37. Mikels, A. J. & Nusse, R. Purified Wnt5a protein activates or inhibits β-catenin–TCF signaling depending on receptor context. *PLoS Biol.* **4**, e115 (2006).
38. Hung, T. H. et al. Wnt5A regulates ABCB1 expression in multidrug-resistant cancer cells through activation of the non-canonical PKA/β-catenin pathway. *Oncotarget* **5**, 12273–12290 (2014).
39. Veeman, M. T., Axelrod, J. D. & Moon, R. T. A second canon: functions and mechanisms of β-catenin-independent Wnt signaling. *Dev. Cell* **5**, 367–377 (2003).
40. Desmedt, C. et al. Genomic characterization of primary invasive lobular breast cancer. *J. Clin. Oncol.* **34**, 1872–1881 (2016).
41. Bartosovic, M. et al. N^6-methyladenosine demethylase FTO targets pre-mRNAs and regulates alternative splicing and 3′-end processing. *Nucleic Acids Res.* **45**, 11356–11370 (2017).
42. Ji, Z., Lee, J. Y., Pan, Z., Jiang, B. & Tian, B. Progressive lengthening of 3′ untranslated regions of mRNAs by alternative polyadenylation during mouse embryonic development. *Proc. Natl Acad. Sci. USA* **106**, 7028–7033 (2009).
43. Gonsalves, F. C. et al. An RNAi-based chemical genetic screen identifies three small-molecule inhibitors of the Wnt/wingless signaling pathway. *Proc. Natl Acad. Sci. USA* **108**, 5954–5963 (2011).
44. Tan, A., Dang, Y., Chen, G. & Mo, Z. Overexpression of the fat mass and obesity associated gene (FTO) in breast cancer and its clinical implications. *Int. J. Clin. Exp. Pathol.* **8**, 13405–13410 (2015).
45. Pastushenko, I. et al. Identification of the tumour transition states occurring during EMT. *Nature* **556**, 463–468 (2018).
46. Zhang, Y. & Weinberg, R. A. Epithelial-to-mesenchymal transition in cancer: complexity and opportunities. *Front. Med.* **12**, 361–373 (2018).
47. Lin, X. et al. RNA m^{6}A methylation regulates the epithelial mesenchymal transition of cancer cells and translation of Snail. *Nat. Commun.* **10**, 2065 (2019).
48. Rao, V. K. et al. Phosphorylation of Tet3 by cdk5 is critical for robust activation of *BRN2* during neuronal differentiation. *Nucleic Acids Res.* **48**, 1225–1238 (2020).
49. Shi, F. T. et al. Ten-eleven translocation 1 (Tet1) is regulated by *O*-linked *N*-acetylglucosamine transferase (Ogt) for target gene repression in mouse embryonic stem cells. *J. Biol. Chem.* **288**, 20776–20784 (2013).
50. Blaschke, K. et al. Vitamin C induces Tet-dependent DNA demethylation and a blastocyst-like state in ES cells. *Nature* **500**, 222–226 (2013).
51. Losman, J. A. & Kaelin, W. G. What a difference a hydroxyl makes: mutant IDH, (*R*)-2-hydroxyglutarate, and cancer. *Genes Dev.* **27**, 836–852 (2013).
52. Beerling, E. et al. Plasticity between epithelial and mesenchymal states unlinks EMT from metastasis-enhancing stem cell capacity. *Cell Rep.* **14**, 2281–2288 (2016).

53. Liu, J. et al. Landscape and regulation of m^{6}A and m^{6}Am methylome across human and mouse tissues. *Mol. Cell* **77**, 426–440 (2020).
54. Clevers, H. & Nusse, R. Wnt/β-catenin signaling and disease. *Cell* **149**, 1192–1205 (2012).
55. Pai, S. G. et al. Wnt/β-catenin pathway: modulating anticancer immune response. *J. Hematol. Oncol.* **10**, 101 (2017).
56. Mukherjee, N. & Panda, C. K. Wnt/β-catenin signaling pathway as chemotherapeutic target in breast cancer: an update on pros and cons. *Clin. Breast Cancer* **20**, 361–370 (2020).
57. Tian, T. V. et al. Identification of novel TMPRSS2:ERG mechanisms in prostate cancer metastasis: involvement of MMP9 and PLXNA2. *Oncogene* **33**, 2204–2214 (2014).
58. Yuan, B. F. Liquid chromatography–mass spectrometry for analysis of RNA adenosine methylation. *Methods Mol. Biol.* **1562**, 33–42 (2017).
59. Ross, R., Cao, X., Yu, N. & Limbach, P. A. Sequence mapping of transfer RNA chemical modifications by liquid chromatography tandem mass spectrometry. *Methods* **107**, 73–78 (2016).
60. Lánczky, A. et al. miRpower: a web-tool to validate survival-associated miRNAs utilizing expression data from 2178 breast cancer patients. *Breast Cancer Res. Treat.* **160**, 439–446 (2016).
61. Curtis, C. et al. The genomic and transcriptomic architecture of 2,000 breast tumours reveals novel subgroups. *Nature* **486**, 346–352 (2012).
62. Varambally, S. et al. Integrative genomic and proteomic analysis of prostate cancer reveals signatures of metastatic progression. *Cancer Cell* **8**, 393–406 (2005).
63. Rokavec, M., Kaller, M., Horst, D. & Hermeking, H. Pan-cancer EMT-signature identifies RBM47 down-regulation during colorectal cancer progression. *Sci. Rep.* **7**, 4687 (2017).
64. Chen, S. et al. AfterQC: automatic filtering, trimming, error removing and quality control for fastq data. *BMC Bioinformatics* **18**, 80 (2017).
65. Bolger, A. M., Lohse, M. & Usadel, B. Trimmomatic: a flexible trimmer for Illumina sequence data. *Bioinformatics* **30**, 2114–2120 (2014).
66. Dobin, A. et al. STAR: ultrafast universal RNA-seq aligner. *Bioinformatics* **29**, 15–21 (2013).
67. Love, M. I., Huber, W. & Anders, S. Moderated estimation of fold change and dispersion for RNA-seq data with DESeq2. *Genome Biol.* **15**, 550 (2014).
68. Anders, S., Pyl, P. T. & Huber, W. HTSeq—a Python framework to work with high-throughput sequencing data. *Bioinformatics* **31**, 166–169 (2015).
69. Subramanian, A. et al. Gene set enrichment analysis: a knowledge-based approach for interpreting genome-wide expression profiles. *Proc. Natl Acad. Sci. USA* **102**, 15545–15550 (2005).
70. Lee, J. Y., Yeh, I., Park, J. Y. & Tian, B. PolyA_DB 2: mRNA polyadenylation sites in vertebrate genes. *Nucleic Acids Res.* **35**, D165–D168 (2007).
71. Zhang, Y. et al. Model-based analysis of ChIP–seq (MACS). *Genome Biol.* **9**, R137 (2008).
72. Quinlan, A. R. & Hall, I. M. BEDTools: a flexible suite of utilities for comparing genomic features. *Bioinformatics* **26**, 841–842 (2010).
73. Bailey, T. L. et al. MEME SUITE: tools for motif discovery and searching. *Nucleic Acids Res.* **37**, W202–W208 (2009).
74. Veeman, M. T., Slusarski, D. C., Kaykas, A., Louie, S. H. & Moon, R. T. Zebrafish prickle, a modulator of noncanonical Wnt/Fz signaling, regulates gastrulation movements. *Curr. Biol.* **13**, 680–685 (2003).
75. Metzger-Filho, O. et al. Genomic grade adds prognostic value in invasive lobular carcinoma. *Ann. Oncol.* **24**, 377–384 (2013).
76. Van Grembergen, O. et al. Portraying breast cancers with long noncoding RNAs. *Sci. Adv.* **2**, e1600220 (2016).

Acknowledgements

J.J. was supported by the Belgian 'Fonds de la Recherche Scientifique' (FNRS) postdoctoral fellowship, E. Collignon was supported by the L'Oréal 'For Women In Science' fellowship and by the Belgian FNRS and Y.J. was supported by the China Scholarship Council (CSC) postdoctoral fellowship. C.A.W., M.B., B.H. and G.D. were supported by the Belgian FNRS. N.K.S. was supported by the ULB Foundation. F.F. is a ULB Professor. F.F.'s lab was funded by grants from the FNRS and Télévie, the 'Action de Recherche Concertée' (ARC; AUWB-2018-2023 ULB-No 7), Wallon Region grants (U-CAN-REST, INTREPID), an FNRS Welbio grant, the ULB Foundation and the Belgian Foundation Against Cancer (FCC 2016-086 FAF-F/2016/872). P.C. and A.C. are Senior Research Associate and Research Director at the FNRS, respectively. C.S. is a research director at the FNRS and his lab is supported by grants from the FNRS. P.A.L. was supported by the National Institutes of Health (GM 058843). Trace is supported by the 'Belgian Foundation Against Cancer' and, as a part of the EurOPDX infrastructure, by EDIReX a Horizon 2020 grant agreement 731105. PET–CT acquisition was performed at the nuMix-CMMI, which is supported by the European Regional Development Fund (ERDF) and the Walloon Region.

Author contributions

J.J., E. Collignon and F.F. designed experiments and interpreted data. J.J., E. Collignon, C.A.W. and Y.J. performed in vitro phenotypic assays. E. Calonne performed m^{6}A-seq and paired-end RNA-seq experiments. C.A.W., J.J., E. Collignon, B.H., P.P., K.S., P.C. and A.C. performed RNAi and overexpression experiments as well as dot blots, western blots and RT–qPCR. S.G., C.D., Y.B., F.R., J.L.C., M.D.C., X.L., L.T., K.W.G. and C.S. provided human biopsies/data and helped with analysis of these samples. P.A.L., R.L.R. and B.F.Y. performed mass spectrometry experiments. M.K., R.M., R.D., M.G. and G.G. performed mouse xenograft experiments. Z.W. analyzed and interpreted the FDG PET experiments. L.R., E.L. and J.C.M. designed and performed PDX experiments. M.B., G.D., N.K.S., A.K. and G.M. performed bioinformatics analyses. F.F. directed the study and J.J., E. Collignon and F.F. wrote the manuscript.

Competing interests

F.F. is a cofounder of Epics Therapeutics, Belgium. The other authors declare no competing interests.

Additional information

Extended data is available for this paper at https://doi.org/10.1038/s43018-021-00223-7.

Supplementary information The online version contains supplementary material available at https://doi.org/10.1038/s43018-021-00223-7.

Correspondence and requests for materials should be addressed to F.F.

Peer review information *Nature Cancer* thanks the anonymous reviewers for their contribution to the peer review of this work.

Reprints and permissions information is available at www.nature.com/reprints.

Publisher's note Springer Nature remains neutral with regard to jurisdictional claims in published maps and institutional affiliations.

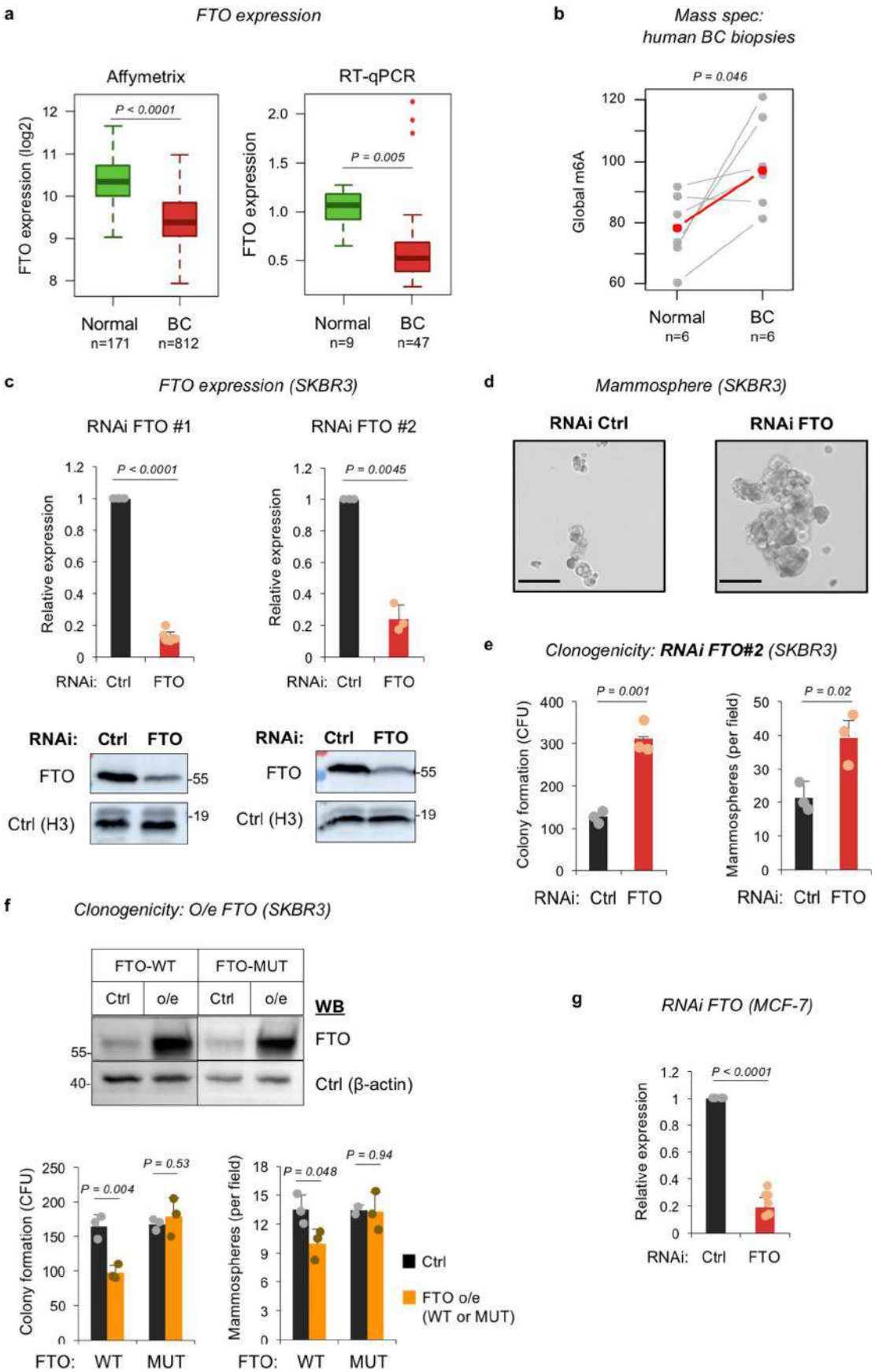

Extended Data Fig. 1 | See next page for caption.

Extended Data Fig. 1 | *FTO* downregulation promotes tumorigenesis in breast cancer. a, *FTO* expression in the Affymetrix data meta-analysis cohort (left, 171 normal vs. 812 tumor breast tissues, p = 5e-50). RT-qPCR quantification of *FTO* in an in-house cohort (right, 9 normal vs. 47 tumor breast tissues, p = 0.005), normalized to *ACTB* and *SDHA*. The box defines the IQR split by the median, with whiskers extending to the most extreme values within 1.5×IQR beyond the box. *P* values calculated by two-tailed t-test. **b**, Quantification of m6A levels by mass spectrometry in paired human normal and tumor breast samples (n = 6 per group, pairs connected with line, red dots represent the group medians, two-tailed paired t-test, p = 0.046). **c**, Validation of *FTO* depletion by two shRNAs in SKBR3 cells by RT-qPCR (upper panel, mean + SD, $p_{RNAi\#1}$ = 6e-10; $p_{RNAi\#2}$ = 0.0045, $n_{RNAi\#1}$ = 7; $n_{RNAi\#2}$ = 3), normalized to *ACTB* and *SDHA*) and western blotting (lower panel, representative of n = 3 independent replicates with histone H3 as loading control). *P* values calculated by two-tailed paired *t*-test. **d**, Light microscopy imaging of mammospheres formed by RNAi Ctrl and RNAi *FTO* SKBR3 cells with scale bar of 100 μm (representative of n = 3 independent experiments). **e**, Effects of *FTO* knockdown on colony-forming capacity (left, *P* = 0.001) and mammosphere-forming capacity (right, *P* = 0.02) in SKBR3 cells with a second shRNA (RNAi *FTO* #2). Data from n = 3 technical replicates (mean + SD) within a single experiment, representative of 3 biologically independent experiments provided as Source Data. *P* values calculated by two-tailed *t*-test. **f**, Representative western blot of doxycycline-induced overexpression of wild-type FTO (FTO-WT) and of a catalytically inactive FTO mutant (FTO-MUT) in SKBR3 cells (upper panel) with β-actin as loading control (n = 3). Effect of FTO-WT and FTO-MUT overexpression on colony formation and mammosphere formation in SKBR3 cells (bottom). Data from n = 3 technical replicates (mean + SD) within a single experiment, representative of 3 and 2 biologically independent experiments, respectively, provided as Source Data. *P* values calculated by two-tailed *t*-test, as indicated. **g**, *FTO* depletion by shRNA in breast cancer MCF7 cells (n = 6) by RT-qPCR. Data as mean + SD, normalized to *ACTB* and *SDHA*. *P* values calculated by two-tailed paired *t*-test (p = 4e-6).

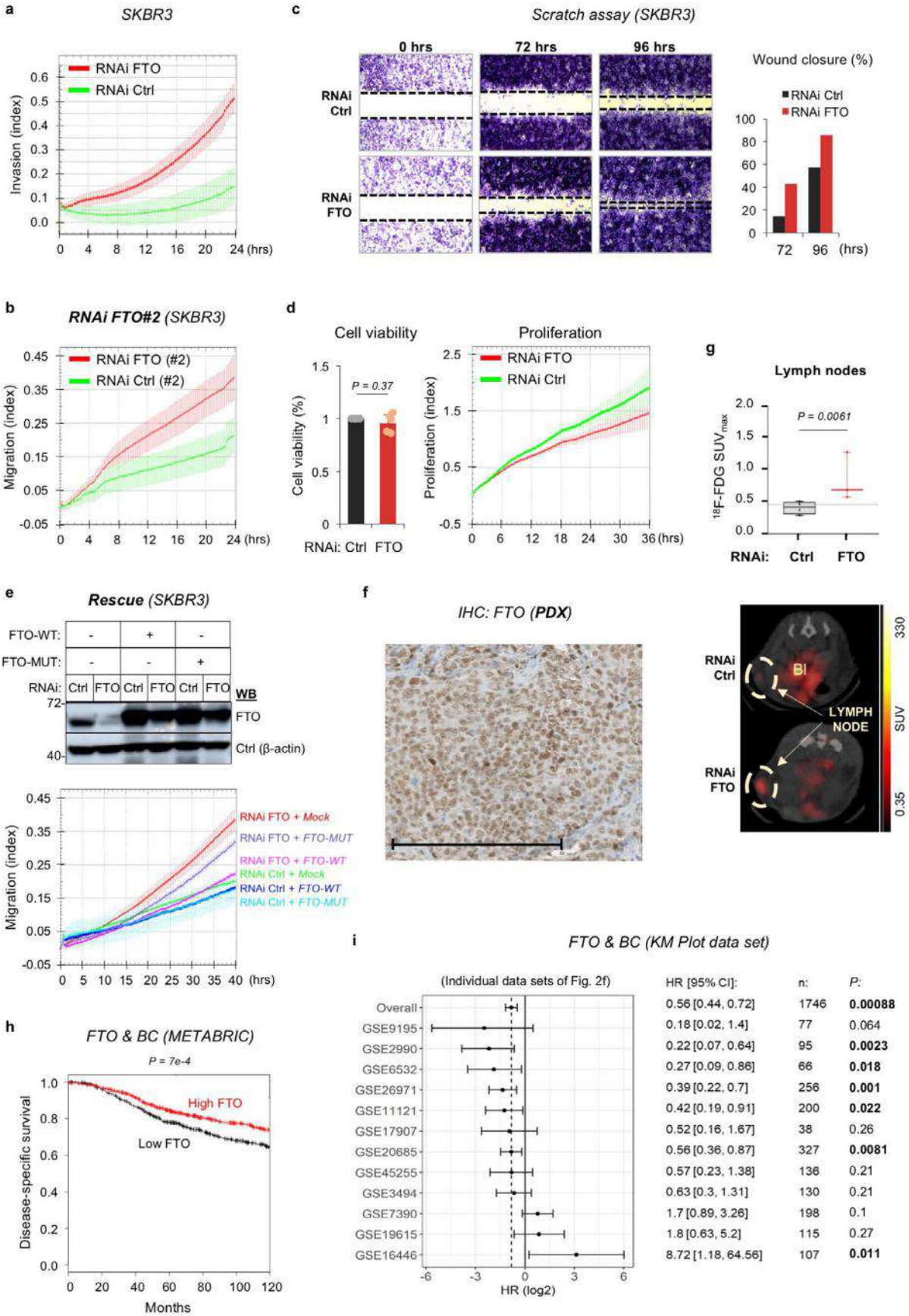

Extended Data Fig. 2 | See next page for caption.

Extended Data Fig. 2 | Depletion of *FTO* promotes breast cancer cell motility and metastases. a-b, Real-time chemotactic invasion (**a**) and migration (**b**) of RNAi *FTO* (red, shRNA #1 and #2, respectively) and RNAi control SKBR3 cells (green). **c**, Wound scratch assay performed with RNAi Ctrl and RNAi *FTO* SKBR3 cells. Representative pictures (left) with quantification of wound closure (as percentage of the width at 0 h, right). Data from a single experiment, representative of n = 2 biologically independent experiments provided as Source Data. **d**, Cell viability by MTT assay (left, mean + SD, n = 5, two-tailed paired t-test, p = 0.37) and real-time proliferation (right) of *FTO*-depleted and control SKBR3 cells. **e**, Western blotting of FTO depletion and rescue by overexpression of wild-type FTO (FTO-WT) or a catalytically inactive FTO mutant (FTO-MUT) in SKBR3 cells (upper panel, n = 3 with β-actin as loading control) and real-time chemotactic migration (lower panel). **f**, Expression of FTO in PDX shown by immunochemistry. Representative image of tissue sections with scale bar of 250 μm (n = 3). **g**, Metabolism imaging with ^{18}F-FDG PET of subiliac lymph nodes xenograft mice bearing RNAi Ctrl (black, n = 4) or RNAi *FTO* (red, n = 5) SKBR3 tumors. Representative images (9 weeks after inoculation) are shown (pathological uptake in LN encircled; physiological uptake in bladder (Bl)). The box defines the IQR split by the median, with whiskers extending to the most extreme values within 1.5×IQR beyond the box. *P*-value calculated by two-tailed *t*-test (*P* = 0.0061). **h**, Kaplan-Meier based on *FTO* expression and disease-specific survival in the breast cancer METABRIC cohort (n(high FTO) = 660, n(low FTO) = 661, logrank test, *P* = 7e-4). **i**, Forest plot showing association between *FTO* expression and distant-metastasis-free survival in breast cancer. Data shown as hazard ratio (log_2), with 95% confidence interval, for both the aggregate KM Plot data set ('overall', presented in Fig. 2f) and individual cohorts. The number of samples (n) and *P*-values (calculated by two-sided logrank tests, in bold if $P < 0.05$) are indicated for each cohort. Data for (**a**), (**b**), (**d**), (**e**) are from n = 3 technical replicates (mean + SD) within a single experiment, representative of 3 biologically independent experiments (except for (**e**): 2 replicates). Independent repeats have been deposited on the Figshare repository (DOI: 10.6084/m9.figshare.14602965).

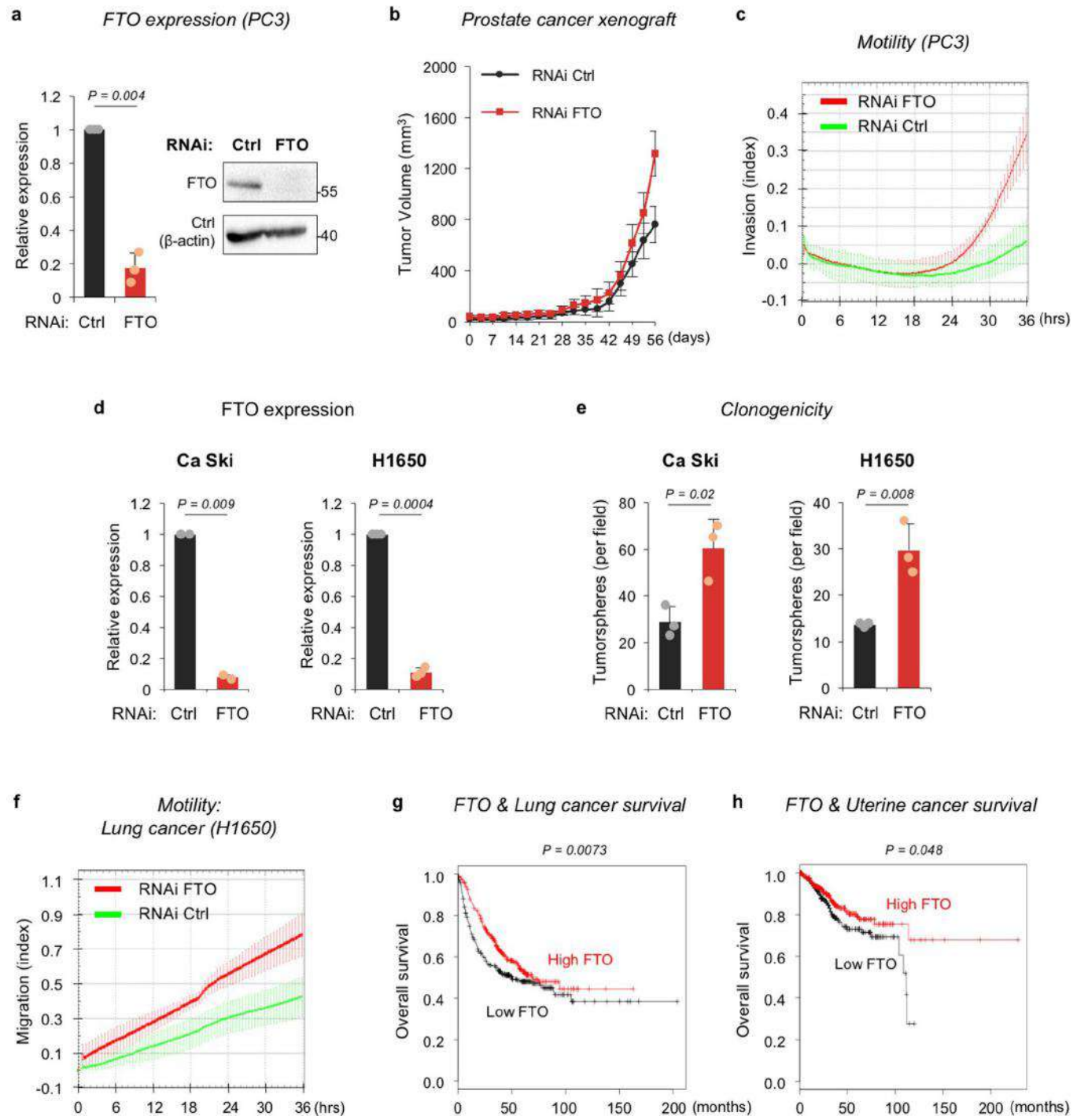

Extended Data Fig. 3 | *FTO* depletion in prostate, cervical and lung cancers. a, *FTO* depletion by shRNA in PC3 prostate cancer cells by RT-qPCR (left). Mean + SD from 3 independent experiments, normalized to *ACTB* and *SDHA*. *P* value calculated by two-tailed paired *t*-test ($P = 0.004$). Representative western blot (right) of FTO depletion in PC3 cells (n = 3) with β-actin as loading control. **b**, Nude mice were injected subcutaneously with PC3 prostate cells and tumors was monitored every two days (n = 6 tumors per group; mean ± SEM, p = 0.0002, two-way ANOVA). **c**, Real-time chemotactic invasion of RNAi *FTO* (red) and RNAi control PC3 cells (green). **d**, *FTO* depletion by shRNA in Ca Ski cervical cancer cells (left, n = 3, $P = 0.009$) and H1650 lung cancer cells (right, n = 3, p = 0.0004) by RT-qPCR. Data as mean + SD, normalized to *ACTB* and *SDHA*. *P* values calculated by two-tailed paired t-test. **e**, Effects of *FTO* knockdown on tumorsphere-forming capacity in Ca Ski (left, $P = 0.02$) and H1650 cells (right, p = 0.008). Data from n = 3 technical replicates (mean + SD) within a single experiment, representative of 2 biologically independent experiments provided as Source Data. *P* values calculated by two-tailed t-test. **f**, Real-time chemotactic migration of *FTO*-depleted (red) and control (green) H1650 cells. **g-h**, Kaplan-Meier curves showing the overall survival of patients with either high-*FTO* or low-*FTO* lung tumors (n(high *FTO*) = 333, n(low *FTO*) = 326, logrank test, $P = 0.0073$) (**g**) or uterine tumors (n(high *FTO*) = 310, n(low *FTO*) = 232, logrank test, $P = 0.048$) (**h**). Motility data in (**c**), (**f**) from n = 3 technical replicates (mean + SD) within a single experiment, representative of 2 and 3 biologically independent experiments, respectively. Independent repeats have been deposited on the Figshare repository (DOI: 10.6084/m9.figshare.14602971).

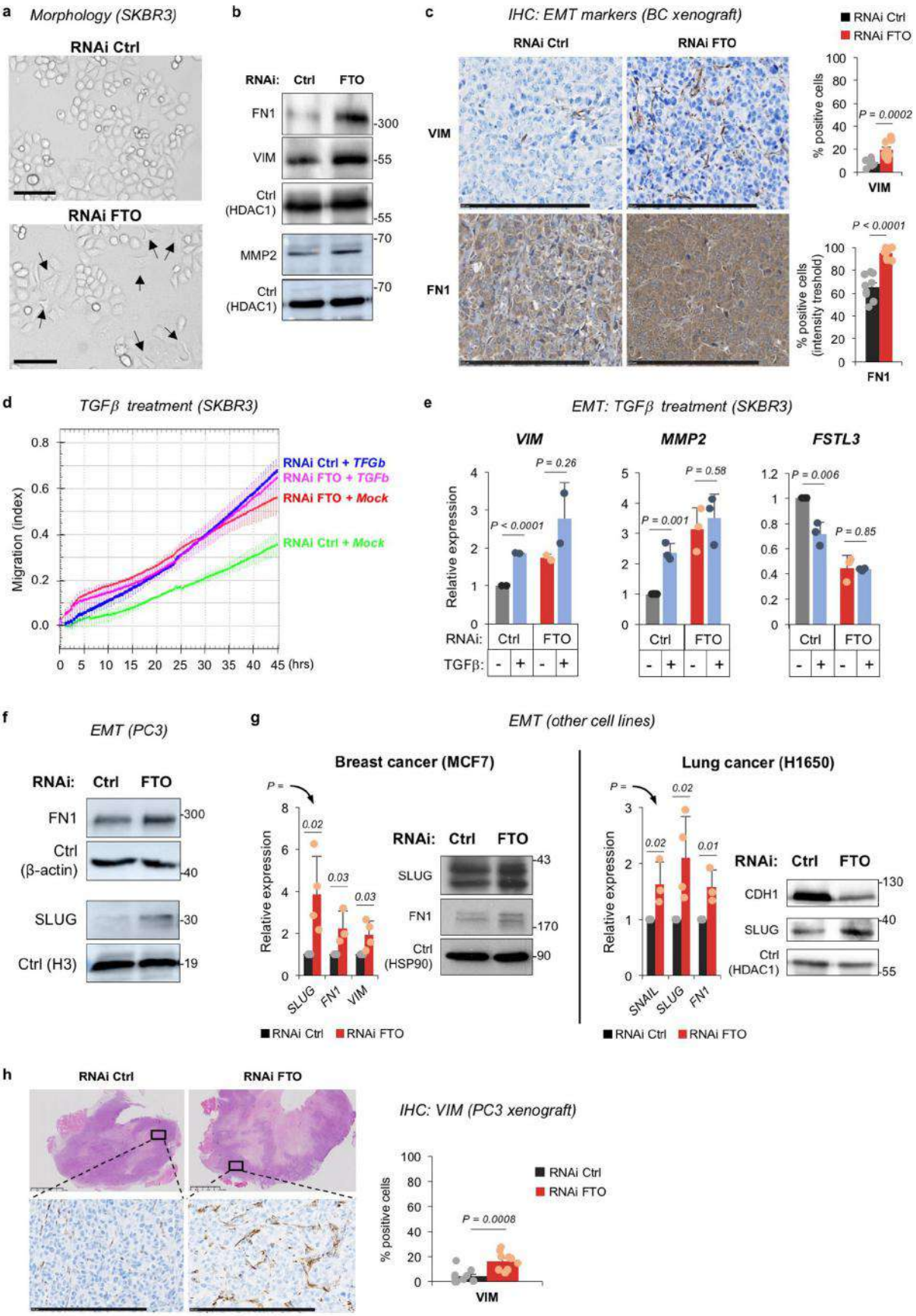

Extended Data Fig. 4 | See next page for caption.

Extended Data Fig. 4 | *FTO* downregulation promotes EMT in several cancers. a, Representative light microscopy imaging of RNAi Ctrl or RNAi *FTO* SKBR3 cells (n = 3 independent experiments). Cells displaying elongated morphology and extended pseudopodia are indicated with arrows. Scale bars represent 50μm. **b**, Representative western blot of mesenchymal EMT markers in *FTO*-depleted (RNAi *FTO*) and control (RNAi Ctrl) SKBR3 cells (n = 3) with HDAC1 as loading control. **c**, Immunochemistry staining of EMT markers in SKBR3 xenografted tumors (from Fig. 1e at endpoint). Percent VIM and FN1 positive cells (n = 3 fields × 3 tumors per group; mean + SEM). *P*-values calculated by two-tailed *t*-test ($p_{VIM} = 0.0002$; $p_{FN1} < 0.0001$). **d**, Real-time chemotactic migration of *FTO*-depleted and control SKBR3 cells in the absence and presence of TGFβ. Data from n = 3 technical replicates (mean + SD) within a single experiment, representative of 3 biologically independent experiments. Independent repeats have been deposited on the Figshare repository (DOI: 10.6084/m9.figshare.14602986). **e**, Relative gene expression of mesenchymal (*VIM*, *MMP2*) and epithelial (*FSTL3*) EMT marker genes, as estimated by RT-qPCR in SKBR3 cells following RNAi of FTO, treated or not with TGFβ. Mean + SD from n = 3 independent experiments, normalized to *ACTB* and *SDHA*. *P* values calculated by two-tailed paired *t*-test as indicated. **f**, Representative western blot of mesenchymal EMT markers FN1 and SLUG in *FTO*-depleted and control PC3 cells (n = 3) with β-actin and histone H3 as loading controls. **g**, Relative gene expression of mesenchymal EMT marker genes, as estimated by RT-qPCR in MCF7 (left, n = 4 except for $n_{FN1} = 3$) and H1650 (right, n = 3 except for $n_{SLUG} = 4$) cells following RNAi of FTO. Mean + SD, normalized to *ACTB* and *SDHA*. P values calculated by two-tailed t-test. Representative western blot of mesenchymal EMT markers FN1, CDH1 and SLUG in *FTO*-depleted and control MCF7 (left) and H1650 (right) cells (n = 3) with HSP90 and HDAC1 as loading controls. **h**, Immunochemistry staining of VIM in PC3 xenografted tumors (from Fig. 3c at endpoint). Percent VIM positive cells (n = 3 fields × 3 tumors per group; mean + SEM). *P*-value calculated by two-tailed *t*-test (p = 0.0008). Scale bars represent 250μm.

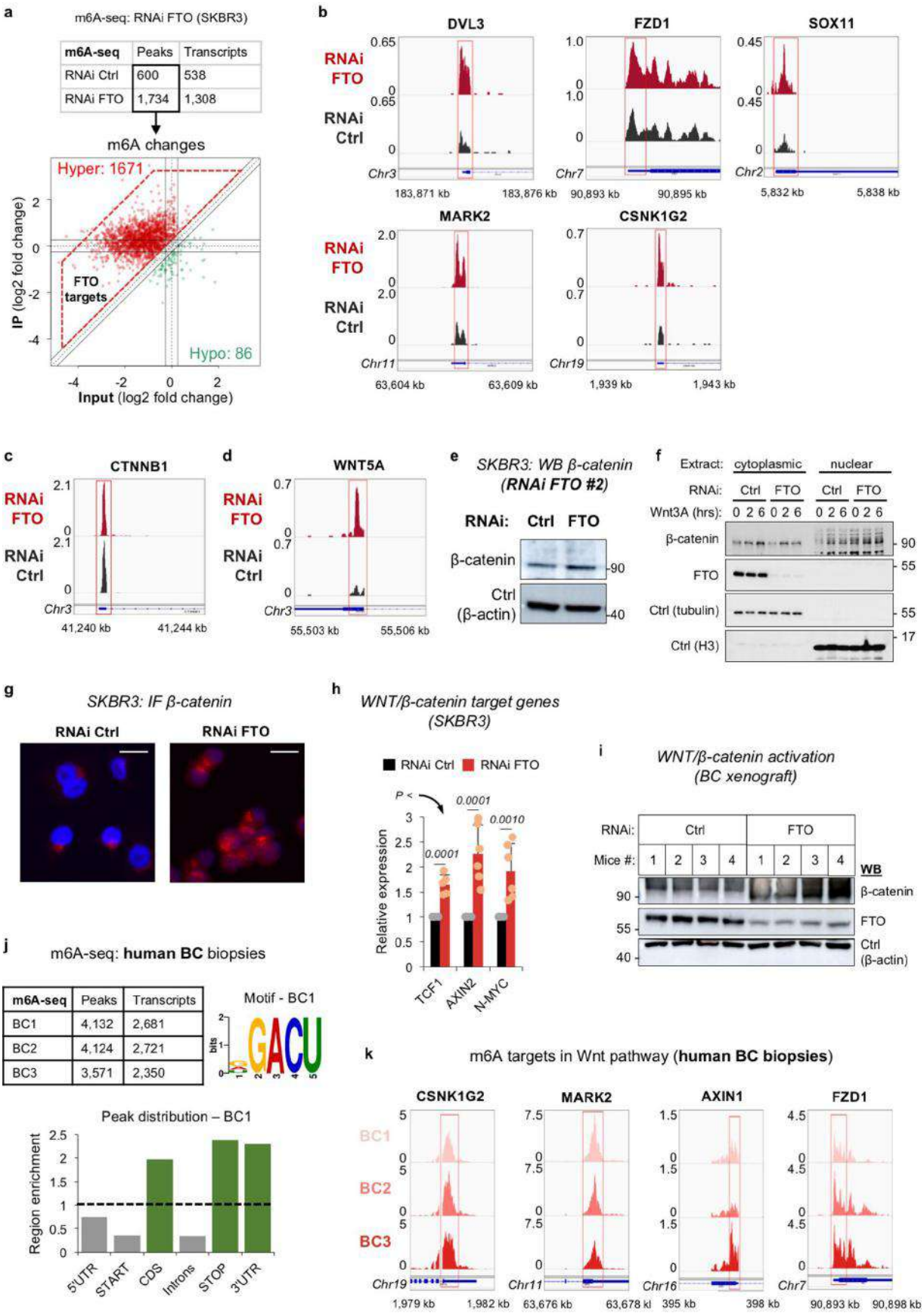

Extended Data Fig. 5 | See next page for caption.

Extended Data Fig. 5 | *FTO* loss upregulates Wnt/β-catenin signaling in breast and prostate cancers. a, Numbers of m6A peaks and related transcripts identified by m6A-seq in RNAi Ctrl and RNAi *FTO* SKBR3 cells (upper panel, two independent biological replicates). Scatterplot displaying differentially m6A-methylated peaks (lower panel, hyper and hypo = peaks with increased and decreased m6A in *FTO*-depleted cells, respectively). **b-d**, Visualization of the IP m6A signal in RNAi *FTO* and RNAi Ctrl SKBR3 cells at the *DVL3*, *FZD1*, *SOX11*, *MARK2*, *CSNK1G2* (**b**), *CTNNB1* (**c**), and *WNT5A* (**d**) transcripts. **e**, Representative western blot of β-catenin in RNAi *FTO* #2 and RNAi Ctrl #2 SKBR3 cells with β-actin as loading control (n = 3). **f**, Representative western blot of cytoplasmic and nuclear β-catenin in RNAi *FTO* and RNAi Ctrl SKBR3 cells (n = 3). Loading controls: β-Tubulin (cytoplasmic) and histone H3 (nuclear). Wnt3a treatment as positive control for nuclear translocation of β-catenin. **g**, Representative immunofluorescence staining of β-catenin (red) and DAPI (blue) in RNAi Ctrl and RNAi *FTO* SKBR3 (n = 3). Scale bars represent 20μm. **h**, Relative gene expression of Wnt/β-catenin targets measured by RT-qPCR in SKBR3 cells. Mean + SD from n = 6 independent replicates (except for n(*TCF1*) = 5), normalized to *ACTB* and *SDHA*. Two-tailed paired t-tests: $P_{TCF1} < 0.0001$; $P_{AXIN2} = 0.0001$; $P_{NMYC} = 0.001$. **i**, Western blot of total β-catenin in RNAi *FTO* vs. RNAi Ctrl from SKBR3 xenografted tumors in mice (n = 4 per group) with β-actin as loading control. **j**, Numbers of m6A peaks and related transcripts identified in three human breast cancer biopsies by m6A-seq (upper left panel). The m6A motif (upper right) retrieved from sample BC1 includes the consensus motif DRACH. Bar graph displaying the distribution of m6A peaks relatively to transcriptomic regions (lower panel, representative of sample BC1). **k**, m6A IP signal at transcripts related to the Wnt/β-catenin signaling (*CSNK1G2*, *MARK2*, *AXIN1* and *FZD1*), in three human breast cancer biopsies.

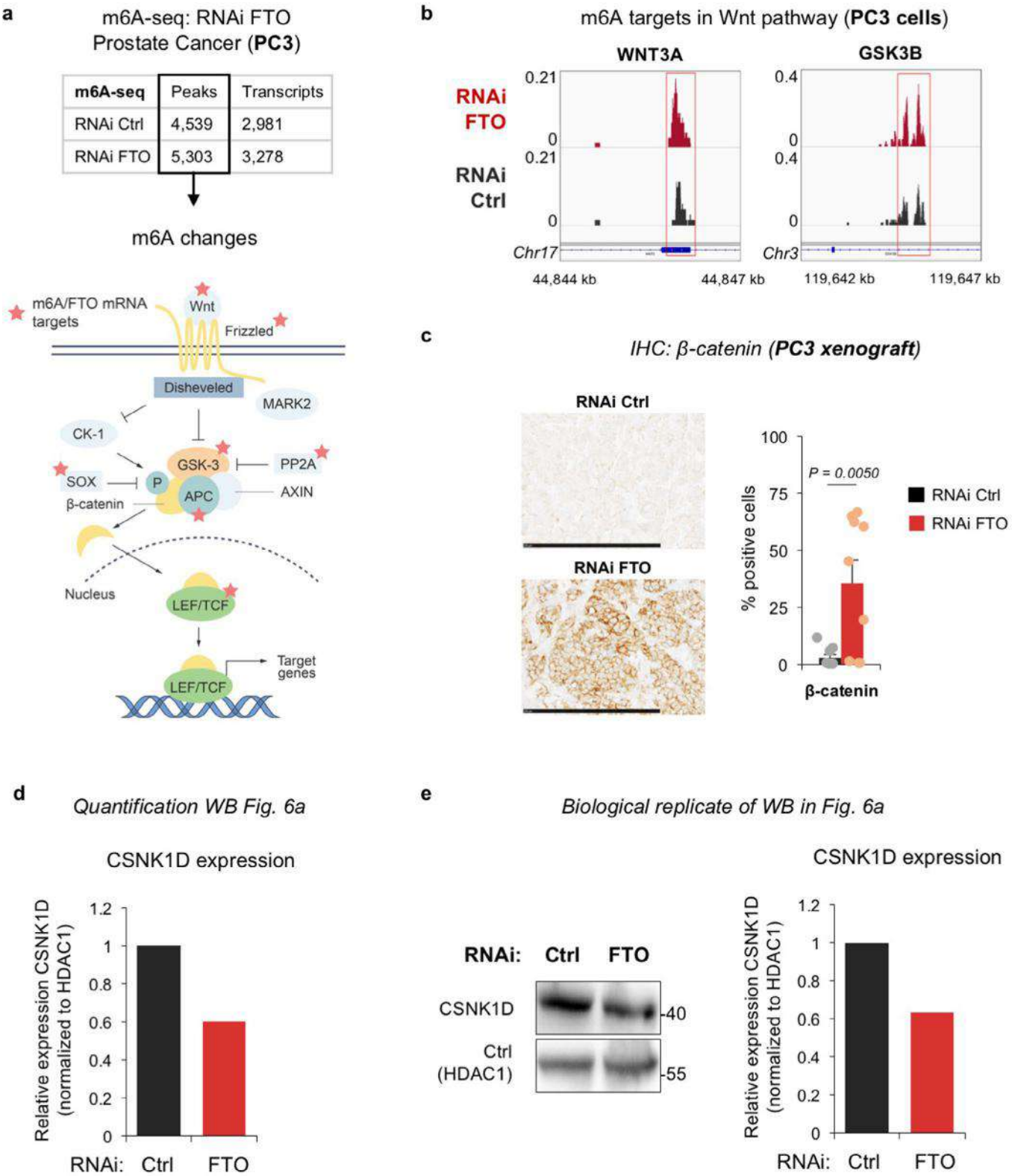

Extended Data Fig. 6 | Regulation of FTO targets. a, Numbers of m6A peaks and related transcripts identified by m6A-seq in RNAi Ctrl and RNAi *FTO* PC3 cells (upper panel, two independent biological replicates). Schematic representation of m^{6}A/FTO mRNA targets (red asterisks) identified within the Wnt/β-catenin signaling pathway (lower panel). **b**, Visualization of the IP m6A signal in RNAi *FTO* and RNAi Ctrl PC3 cells at the *WNT3A* and *GSK3B* transcripts. **c**, Representative immunochemistry staining of β-catenin in PC3 xenografted tumors with scale bar at 250 μm. Percent β-catenin positive cells (right, n = 3 fields × 3 tumors per group; mean + SD). Two-tailed *t*-test, $P = 0.005$. **d**, Relative quantification of the CSNK1D levels in RNAi *FTO* and RNAi Ctrl SKBR3 cells displayed in the western blot shown in Fig. 6a. **e**, Western blot showing the level of CSNK1D in an independent biological replicate of RNAi FTO and RNAi Ctrl SKBR3 cells (left, with HDAC1 as loading control, related to Fig. 6a). Relative quantification of CSNK1D levels (right). Western blot data in (**d-e**) are representative of n = 3 biologically independent experiments and normalized to HDAC1.

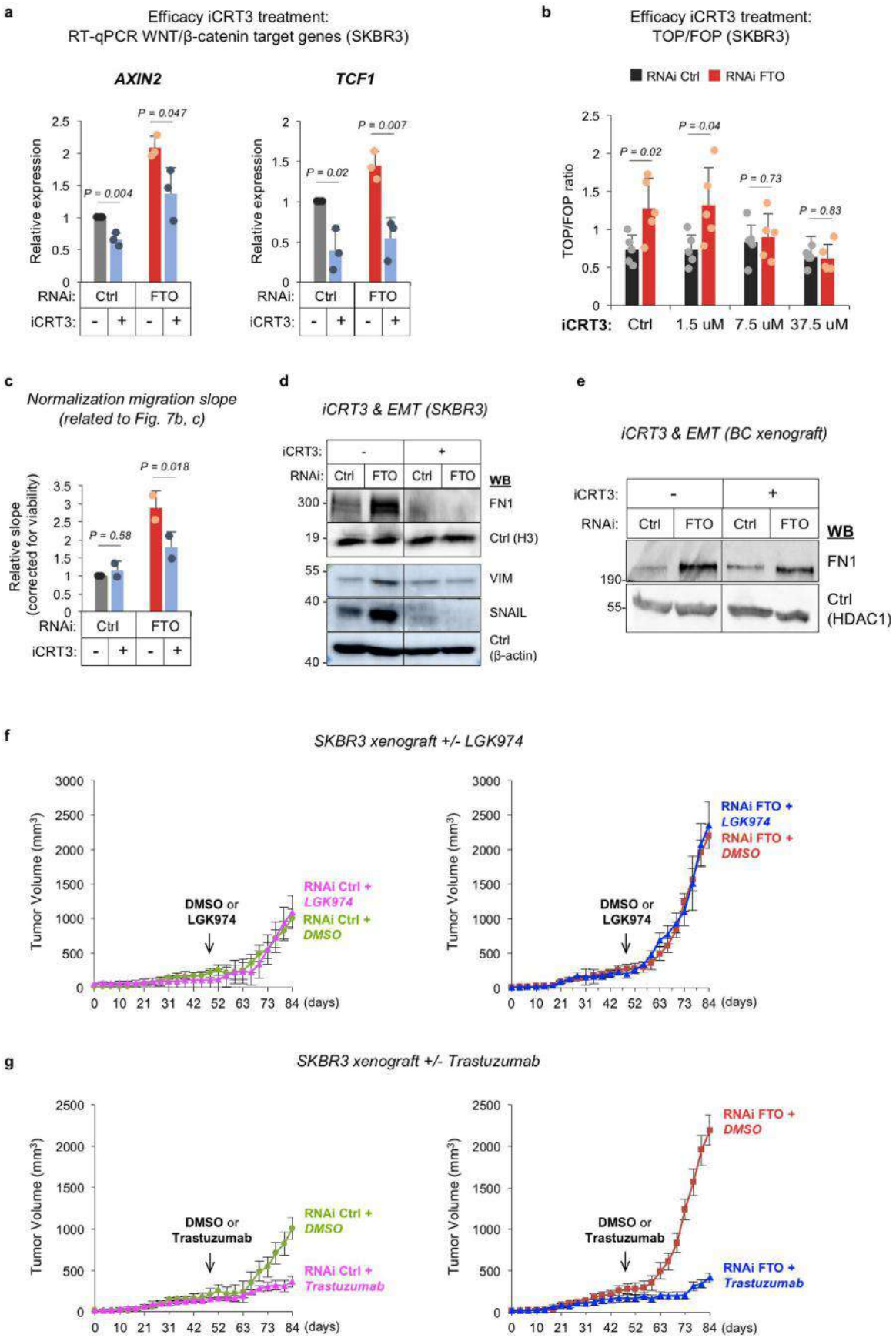

Extended Data Fig. 7 | See next page for caption.

Extended Data Fig. 7 | *FTO*-low tumors are sensitive to WNT inhibitor therapy. a, Relative gene expression of Wnt/β-catenin target genes *AXIN2* and *TCF1*, as estimated by RT-qPCR, in SKBR3 cells following RNAi of *FTO*, treated or not with iCRT3. Mean + SD from 3 independent experiments, normalized to *ACTB* and *SDHA*. *P* values calculated by two-tailed *t*-test, as indicated. **b**, Wnt/β-catenin transcriptional activity, as measured by TOPFlash β-catenin/TCF-LEF reporter assay performed on SKBR3 cells following RNAi of *FTO*, in the absence and presence of iCRT3 (mean + SD, n = 5, iCRT3 doses as indicated). *P* values calculated by two-tailed t-test, as indicated. **c**, The migration capacity, as shown in Fig. 7b, was quantified by the slope of the migration curves and corrected for cell viability (as measured by MTT assay in Fig. 7c, from 2 biologically independent experiments). *P*-values calculated by two-tailed *t*-test (p(RNAi Ctrl)=0.58, p(RNAi *FTO*) = 0.018). **d**, Levels of the mesenchymal EMT marker proteins FN1, VIM and SNAIL in RNAi Ctrl and RNAi *FTO* SKBR3 cells in the absence and presence of iCRT3 (n = 3) with histone H3 and β-actin as loading controls. **e**, Levels of FN1 protein in *FTO*-depleted and control tumors derived from SKBR3 xenografts treated with iCRT3 or vehicle (DMSO), with β-actin as loading control (n = 3 independent experiments). **f**, Nude mice growing tumors from RNAi Ctrl (left) or RNAi *FTO* (right) SKBR3 cells were treated with LGK974 (n = 5 tumors per group, mean ± SEM). *P* values calculated by two-way ANOVA (p(RNAi Ctrl)=0,69; p(RNAi *FTO*) = 0.48). **g**, Nude mice growing tumors from RNAi Ctrl (left) or RNAi *FTO* (right) PC3 cells were treated with or without Trastuzumab (n = 5 tumors per group, mean ± SEM). *P* values calculated by two-way ANOVA, (p(RNAi Ctrl)<0.0001; p(RNAi *FTO*) < 0.0001).

nature research

Corresponding author(s): François Fuks

Last updated by author(s): May 16, 2021

Reporting Summary

Nature Research wishes to improve the reproducibility of the work that we publish. This form provides structure for consistency and transparency in reporting. For further information on Nature Research policies, see our Editorial Policies and the Editorial Policy Checklist.

Statistics

For all statistical analyses, confirm that the following items are present in the figure legend, table legend, main text, or Methods section.

n/a	Confirmed
☐	☒ The exact sample size (*n*) for each experimental group/condition, given as a discrete number and unit of measurement
☐	☒ A statement on whether measurements were taken from distinct samples or whether the same sample was measured repeatedly
☐	☒ The statistical test(s) used AND whether they are one- or two-sided *Only common tests should be described solely by name; describe more complex techniques in the Methods section.*
☒	☐ A description of all covariates tested
☐	☒ A description of any assumptions or corrections, such as tests of normality and adjustment for multiple comparisons
☐	☒ A full description of the statistical parameters including central tendency (e.g. means) or other basic estimates (e.g. regression coefficient) AND variation (e.g. standard deviation) or associated estimates of uncertainty (e.g. confidence intervals)
☐	☒ For null hypothesis testing, the test statistic (e.g. *F*, *t*, *r*) with confidence intervals, effect sizes, degrees of freedom and *P* value noted *Give P values as exact values whenever suitable.*
☒	☐ For Bayesian analysis, information on the choice of priors and Markov chain Monte Carlo settings
☒	☐ For hierarchical and complex designs, identification of the appropriate level for tests and full reporting of outcomes
☐	☒ Estimates of effect sizes (e.g. Cohen's *d*, Pearson's *r*), indicating how they were calculated

Our web collection on statistics for biologists contains articles on many of the points above.

Software and code

Policy information about availability of computer code

Data collection

qPCR data was acquired on the LightCycler480 real-time PCR system (Roche). Western blots and dot blots were developed with the ECL system (Amersham Biosciences) using the ChemiDoc™ Imaging Systems (Bio-Rad). Mass spectrometry data was collected by an AB 3200 QTRAP mass spectrometer (Applied Biosystems, Foster City, CA, USA) or a Thermo Scientific™ QuantivaTM triple quadrupole mass spectrometer, and data were analyzed using Tracefinder 4.1 (Thermo Fisher Scientific) and Qual browser of Xcalibur 3.0 (Thermo Scientific). m6A-Seq and RNA-Seq data were collected by NextSeq500 system (Illumina). IHC slides were imaged with an NDP Slice Scanner (Hamamatsu). Proliferation, migration and invasion were measured with the Real-Time Cell Analyzer (RTCA) Dual Plate (DP) system (xCELLigence, ACEA Biosciences). PET-CT imaging and analysis were conducted with a µPET-CT scanner (nanoScan®PET/CT, Mediso).
Alternative polyA site usage was analyzed using a script adapted from 'roarWrapper_chrBychr.R' (https://github.com/vodkatad/roar/blob/master/inst/examples/).

Data analysis

- Graphpad prism 7 and the computing environment R v3.5.1 were used for statistics.
- ImageJ software was used for signal quantification.
- The raw sequencing data was analysed with FastQC v0.11.4.
- Low-complexity reads were removed with the AfterQC tool v0.9.1.
- Adapters on reads were processed with Trimmomatic v0.36.
- Preprocessed reads were mapped against the human reference genome (hg19) with STAR v2.5.1b (RNA-Seq and m6A-Seq).
- Peak regions were identified by applying the MACS2 peak-calling tool v2.1.0.20150731.
- Bedtools v2.25.0 was used to compute peaks overlap and extract peak sequences.
- Peaks were visualized in IGV tool v2.3.82(130)
- Motif analysis was performed with the meme-suite v4.11.1.
- Gene ontology was performed with Ingenuity Pathway Analysis v01-07.
- Gene expression was computed with the HTseq tool v0.6.1p1.
- Differential analysis was performed with the DESeq2 tool v3.11.
- Alternative polyadenylation usage was analysed using ROAR v1.16.0

- Gene-set enrichment analyses were performed using GSEA v3.0
- Code supporting this study are available at a dedicated Github repository [https://github.com/martinBizet/m6A_FTO_cancer].

For manuscripts utilizing custom algorithms or software that are central to the research but not yet described in published literature, software must be made available to editors and reviewers. We strongly encourage code deposition in a community repository (e.g. GitHub). See the Nature Research guidelines for submitting code & software for further information.

Data

Policy information about availability of data

All manuscripts must include a data availability statement. This statement should provide the following information, where applicable:

- Accession codes, unique identifiers, or web links for publicly available datasets
- A list of figures that have associated raw data
- A description of any restrictions on data availability

Sequencing data that support the findings of this study have been deposited in the Gene Expression Omnibus (GEO) repository under accession number GSE128582 (http://ncbi.nlm.nih.gov/geo).

Human cancer data (bladder urothelial carcinoma, breast invasive carcinoma, cervical squamous cell carcinoma and endocervical adenocarcinoma, glioblastoma multiforme, kidney chromophobe, lung adenocarcinoma and lung squamous cell carcinoma, prostate adenocarcinoma, thyroid carcinoma, and uterine corpus endometrial carcinoma) were derived from the TCGA Research Network: http://cancergenome.nih.gov/. RNA-seq data from TCGA were obtained as normalised FPKM counts from GDC (https://portal.gdc.cancer.gov/repository) and PAM50 subtype information was extracted from UCSC Xena (https://xenabrowser.net). METABRIC expression and clinical data61 were downloaded through the European Genome-Phenome Archive (EGA) (http://www.ebi.ac.uk/ega/, accession number EGAS00000000083). Previously published microarray data that were re-analysed here are available under accession code GSE9195, GSE10780, GSE10810, GSE12276, GSE19615, GSE20711, and GSE21653. Reannotation and processing of Affymetrix Human Genome U133 Plus 2.0 array data was performed as previously detailed76.

The hg19 reference transcriptome (version 85) was obtained from the ensembl portal (ensembl.org). Hallmark gene sets were obtained from MsigDB database (https://www.gsea-msigdb.org/gsea/msigdb). Human polyadenylation sites were obtained from PolyA_DB2 (http://polya.umdnj.edu/PolyA_DB2).

The data underlying Figs 1b, 1d-h, 2c-e, 3a-b, 3d, 3g, 4c, 4e, 5e, 5g, 5j-k, 6e, 7a, 7c, 8b-d and Extended Data Figs 1a-c, 1e-g, 2c-d, 2g, 3a-b, 3d-e, 4c, 4e, 4g-h, 5h, 6c-e, 7a-c, 7e-f are provided as Source Data files. For motility assays related to Figs 2a-b, 3c, 3e, 7b and Extended Data Figs 2a-b, 2d-e, 3c, 3f, 4d, independent repeats have been deposited on the Figshare repository, under the following DOI: 10.6084/m9.figshare.14602932, 10.6084/m9.figshare.14602944, 10.6084/m9.figshare.14602953, 10.6084/m9.figshare.14602965, 10.6084/m9.figshare.14602971 and 10.6084/m9.figshare.14602986). All other data supporting the findings of this study are available from the corresponding author on reasonable request.

Field-specific reporting

Please select the one below that is the best fit for your research. If you are not sure, read the appropriate sections before making your selection.

☒ Life sciences ☐ Behavioural & social sciences ☐ Ecological, evolutionary & environmental sciences

For a reference copy of the document with all sections, see nature.com/documents/nr-reporting-summary-flat.pdf

Life sciences study design

All studies must disclose on these points even when the disclosure is negative.

Sample size	Sample size, number of replicates, errors bars and statistical tests were chosen based on experience and variability of in vitro studies, and are stated in each figure legend. Unless otherwise indicated, all experiments included technical replicates and were repeated at least three times, using independent rounds of infection for knockdown. No statistical methods were used to predetermine sample sizes. By default, we aimed for three replicates per experiments to allow statistical tests to be performed. Occasionally, additional replicates were made available to us as a result of other experiments and exploited to increase the sample size of a prior assay. For instance, when a new round of infection was validated by RT-qPCR, additional markers were often tested at the same time, resulting in n > 3 for such markers. For in vivo experiments, 3 or more mice were randomized per group, and follow-up experiments were conducted based on the availability of material with a minimum of 3 samples per group. Specifically, for most xenograft experiments, the number was increased to 5-6 mice per group to ensure sufficient material for downstream experiments (qPCR, western blot, IHC). For PET-scan imaging and PDX experiments, numbers were limited (3-5 mice per groups), due to factors such as housing availability, access to mouse purchase and costs. The exact number of mice per group is indicated in the legends of all animal experiments. Experiments performed on residual human biopsy samples were conducted based on the availability of residual material with a minimum of 3 samples per group.
Data exclusions	No data were excluded from analysis.
Replication	All attempts to replicate experiments were successful. Details on replication of each particular experiments are provided in Figure Legends.
Randomization	For each in vitro experiment, a subpopulation of cells was allocated randomly from the parental population of cells without using specific randomization methods. For mice experiments, mice of the same background and same age were purchased together, and allocated randomly to the different arms, without using specific randomization methods. Experiments performed on human residual material were observational only, i.e. group allocation was performed on the basis of a measured

variable (e.g. FTO expression or beta-catenin levels) and not by intervention of the experimenters. Thus randomization was not applicable.

Blinding

Blinding was generally not applied as experimental conditions (e.g. FTO knockdown, Wnt inhibition, etc.) were validated within each experiment through objective quantitative methods (eg. RT-qPCR of relevant markers), and thus were evident. This applies to in vitro experiments, mice experiments, and experiments on human biopsies. It is worth noting that for each experiment, samples of all groups were treated in parallel time to ensure equal conditions.
PET imaging was, however, performed in a blinded manner.

Reporting for specific materials, systems and methods

We require information from authors about some types of materials, experimental systems and methods used in many studies. Here, indicate whether each material, system or method listed is relevant to your study. If you are not sure if a list item applies to your research, read the appropriate section before selecting a response.

Materials & experimental systems

n/a	Involved in the study
☐	☒ Antibodies
☐	☒ Eukaryotic cell lines
☒	☐ Palaeontology and archaeology
☐	☒ Animals and other organisms
☐	☒ Human research participants
☒	☐ Clinical data
☒	☐ Dual use research of concern

Methods

n/a	Involved in the study
☒	☐ ChIP-seq
☒	☐ Flow cytometry
☒	☐ MRI-based neuroimaging

Antibodies

Antibodies used

-CD31 (Cell Marque, 131M, clone JC70) for IHC (ready-to-use)
-Cleaved Caspase 3 (Abcam, ab2302) for IHC (diluted 1/100)
-CSNK1D (BEYHYL, A302-136A-T) for western blot (diluted 1/500)
-FN1 (Sigma Aldrich, HPA027066) for western blot (diluted 1/500) and IHC (diluted 1/100)
-FTO (Abcam, ab124892, clone EPR6895) for western blot (diluted 1/1000) and IHC (diluted 1/200)
-HDAC1 (Diagenode, C15410325) for western blot (diluted 1/1000)
-Histone H3 (Abcam, ab70550) for western blot (diluted 1/2000)
-HSP90 (Santa Cruz, Sc-13119) for western blot (diluted 1/2000)
-Ki67 (Dako, M7240, clone MIB-1) for IHC (ready-to-use)
-m6A (Synaptic Systems, 202 003) for m6A-seq (7.8ug per IP)
-MMP2 (Cell Signaling, 13132) for western blot (diluted 1/1000)
-SLUG (Cell Signaling, 9585) for western blot (diluted 1/1000)
-SNAIL (Sigma-Aldrich, HPA069985) for IHC (diluted 1/500)
-SNAIL (Cell Signaling, 3879) for western blot (diluted 1/1000)
-Tubulin (Sigma Aldrich, T6199, clone DM1A) for western blot (diluted 1/500)
-VIM (Sigma Aldrich, HPA001762) for western blot/IHC (diluted 1/2000)
-WNT5A (Cell Signaling, C27E8 2530) for western blot (diluted 1/1000)
-β-actin (Sigma Aldrich, A5316) for western blot (diluted 1/1000)
-β-catenin (Dako, IR70261-2, clone II-7) for immunofluorescence (ready-to-use)
-β-catenin (Santa Cruz, sc-7963, clone E-5) for western blot (diluted 1/500)
- Amersham ECL Rabbit IgG, HRP-linked whole Ab (from donkey) (Sigma, GE Healthcare, #NA934-1ML) as secondary for western blot (diluted 1/5000)
- Amersham ECL Mouse IgG HRP-linked whole Ab (from sheep) (Sigma, GE Healthcare, #NA931-1ML) for as secondary for western blot (diluted 1/5000)
-Alexa Fluor 647 goat anti-mouse IgG1 (Invitrogen, A21240) as secondary for immunofluorescence (diluted 1/1000)

Validation

All antibodies used are commercially available. Based on the information from manufacturer's websites, all primary antibodies are validated.
Anti-CD31 (Cell Marque, 131M) was validated by Alles & Bosslet (J Histochem Cytochem, 1986) using IHC and IP followed by SDS-PAGE. Anti-Cleaved Caspase 3 (Abcam, ab2302) was validated by western blot on recombinant protein and IHC on tissue (see Abcam website). Anti-CSNK1D (BEYHYL, A302-136A-T) was validated by IP-western blot (see Bethyl website). Anti-FN1 (Sigma Aldrich, HPA027066) was used in western blotting and IHC, and tested with a "protein array of 364 human recombinant protein fragments" (see Sigma-Aldrich website). Anti-FTO (Abcam, ab124892) was tested by western blot and IHC, including on FTO-knockout samples (see Abcam website). Anti-HDAC1 (Diagenode, C15410325) was validated by western blot, using HDAC1-siRNA (see Diagenode website). Anti-Histone H3 (Abcam, ab70550) was validated by wester blot, IHC and IF (see Abcam website). Anti-HSP90 (Santa Cruz, Sc-13119) was validated by western blot (see Santa Cruz website). Anti-Ki67 (Dako, M7240) was validated by western blot and IHC (see Dako-Agilent website). Anti-m6A (Synaptic Systems, 202 003) was validated for m6A-seq by Dominissini et al (Nature 2012). Anti-MMP2 (Cell Signaling, 13132), anti-SNAIL (Cell Signaling, 3879) and anti-SLUG (Cell Signaling, 9585) were validated by western blot (see Cell Signaling website). Anti-SNAIL (Sigma-Aldrich, HPA069985) was validated by IHC, and tested with a "protein array of 364 human recombinant protein fragments" (see Sigma-Aldrich website). Anti-Tubulin (Sigma Aldrich, T6199) was tested by western blot (see Sigma-Aldrich website). Anti-VIM (Sigma Aldrich, HPA001762) were validated by western blot and IHC, and tested with a "protein array of 364 human recombinant protein fragments" (see Sigma-Aldrich website). Anti-WNT5A (Cell Signaling, C27E8 2530) was validated by western blot (see Cell Signaling website). Anti-β-actin (Sigma Aldrich, A5316) was validated

by western blot and IHC (see Sigma-Aldrich website). Anti-β-catenin (Dako, IR70261-2) was validated by ELISA and IHC (see Dako-Agilent website). Anti-β-catenin (Santa Cruz, K2017) was validated by western blot, using β-catenin-siRNA (see Santa Cruz website).

Eukaryotic cell lines

Policy information about cell lines

Cell line source(s)	SKBR3, MCF7, Caski and HEK293GP cells were kindly provided by Agnès Noel and Christine Gilles (Université de Liège, Belgium). PC3 cells were kindly provided by Martine Duterque (Université Lille, France). H1650 were kindly provided by Ghanem Ghanem (Bordet Institute).
Authentication	The cell lines used were not authenticated.
Mycoplasma contamination	All cell lines were tested negative for mycoplasma contamination.
Commonly misidentified lines (See ICLAC register)	None.

Animals and other organisms

Policy information about studies involving animals; ARRIVE guidelines recommended for reporting animal research

Laboratory animals	-For xenograft and tail vein injection experiments, five- to six-week-old female nude (nu/nu) mice weighing 17–21 g were purchased from Charles River Laboratories. -For PDX experiments, NMRI nude female mice of minimum 6 weeks of age were obtained from Taconic.
Wild animals	The study did not involve wild animals.
Field-collected samples	The study did not involve samples collected from the field.
Ethics oversight	-Xenograft experiments were performed in accordance with the European Union Guidelines and validated by the local Animal Ethics Evaluation Committee from the ULB (Université Libre de Bruxelles, CEBEA protocol No: 699N). -PDX experiments were conducted according to the guidelines of KU Leuven and had prior approval from the Animal Care and Ethics Committee (project application P038/2015).

Note that full information on the approval of the study protocol must also be provided in the manuscript.

Human research participants

Policy information about studies involving human research participants

Population characteristics	Residual biopsy material was used for the present study: -Frozen diagnostic samples of breast cancer patients (n=40) admitted to Saint-Louis Hospital (Paris, France) between 2009 and 2013 were obtained from the biological resource center at Saint-Louis Hospital. -Frozen prostate cancer samples (n=19) were obtained from a cohort established for a previous study (Tian et al., Oncogene 2014). Samples came from the local tumor tissue bank, C2RC (Centre de Référence Régional en Cancérologie, Lille, France). As our study was performed on residual biopsy material, we did not have access to patient information, aside from gender (female for breast samples, male for prostate samples). Covariate analysis was therefore not possible.
Recruitment	Samples were chosen based on the avalibility of residual material, following the prior collection of samples by the Saint-Louis Hospital (Paris, France) and the C2RC (Lille, France).
Ethics oversight	-For breast cancer, samples were obtained following the Ethics and Legal National French rules (agreement n° DC 2009-929, ANAES, HAS and INCa). -For Prostate Cancer, samples were obtained after approval by the internal review board (CSTMT-042, 27/07/2009). All patients were informed and consent was obtained by the referring physician.

Note that full information on the approval of the study protocol must also be provided in the manuscript.